Universiteit
Leiden
The Netherlands

Chemical control over hemi-indigo photoswitches

Duindam, N.

Citation
Duindam, N. (2026, June 19). *Chemical control over hemi-indigo photoswitches*. Retrieved from https://hdl.handle.net/1887/4306846

Version:	Publisher's Version
License:	Licence agreement concerning inclusion of doctoral thesis in the Institutional Repository of the University of Leiden
Downloaded from:	https://hdl.handle.net/1887/4306846

Note: To cite this publication please use the final published version (if applicable).

CHAPTER 3

Mechanistic Investigation into a Hemi-Indigo Proton Information Ratchet

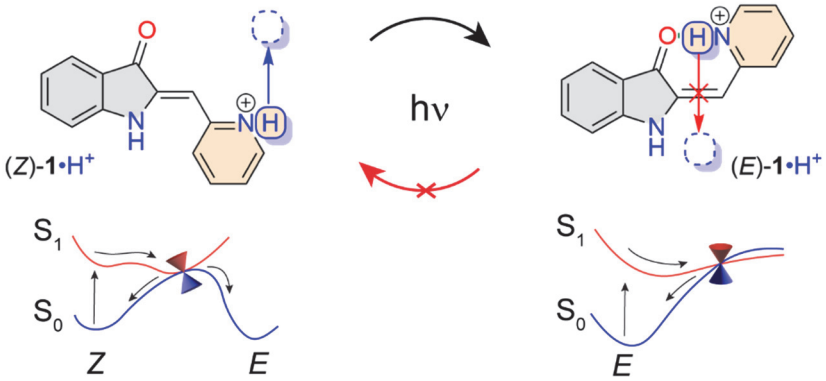

Abstract: The selective inhibition of either forward or backward photoisomerization paths can enable machine-like behavior of a simple bistable switch. Herein, we provide a detailed mechanistic study of the gating of hemi-indigo photochemistry that occurs in the *Z*- and *E*-isomers by (de)protonation. Experiment and computation highlight the profound effect of the intramolecular hydrogen bond on the excited state. Furthermore, the excited-state lifetime of the neutral hydrogen-bonded *Z*-isomer is found to be highly sensitive to deuteration, and this H/D-isotope effect indicates excited-state intramolecular proton transfer. The lack of photoisomerization from the protonated, hydrogen-bonded *E*-isomer is rationalized using high-level QM/MM calculations, highlighting several efficient decay channels on the S_1 surface of the *E*-isomer that are absent for the *Z*-isomer.

The work that is described in this chapter will be published:

N. Duindam, M. S. Bezabih, M. Olivucci, A. M. Brouwer, S. J. Wezenberg, *In preparation.*

3.1 Introduction

The development of molecular switches has significantly impacted a wide range of chemical disciplines.[1–4] Incorporation of these switches into functional molecules allows excellent control over molecular properties by external stimuli. Light is a privileged stimulus as it does not produce waste and gives high spatiotemporal control.[5,6] Generally, photoswitches are toggled between two states with distinct properties. Under irradiation, however, after reaching photoequilibrium, both isomers continuously interconvert with equal rates. This inherent dynamicity is rarely exploited, primarily because the displacements associated with the forward and backward isomerization pathways cancel out. This is in stark contrast with the field of light-driven molecular motors, where unidirectional rotation steered by a stereogenic center enables repetitive net motion.[7–10]

Recently, gating of photochemistry has gained attention as a means to harness the continuous interconversion of photoswitches under light irradiation.[11–14] If an additional chemical stimulus has a different effect on both photoisomers, the two-state cycle can be transformed into a sequence-selective four-state cycle. Profound effects of non-covalent interactions on the photochemistry are abundant in the literature,[15] but are often poorly understood. Ground-state trends, such as mechanical stabilization of one isomer, are frequently invoked, yet, in reality, photochemical properties are ultimately governed by the excited-state potential energy surface (PES). In-depth understanding of competitive de-excitation channels introduced by the intramolecular hydrogen bond can aid in the design of novel gated switches, but may also be of value in the design of highly photostable dyes.[16]

Our group recently developed *N*-heterocyclic hemi-indigo dyes, in which the forward *Z*-to-*E* photoisomerization takes place only when protonated, while the reverse *E*-to-*Z* photoisomerization occurs exclusively in the neutral state.[17] As forward and backward photoisomerization do not occur in the same protonation state, net motion is no longer fully canceled out. In fact, a proton that is displaced in the protonated state (*Z*-to-*E*) has to dissociate before the reverse *E*-to-*Z* photoisomerization can occur. We realized that such a sequence-selective photocycle could lead to the unidirectional displacement of protons (Scheme 1). In the design of the gated *N*-heterocyclic hemi-indigos, we were guided by the empirical observation that photoisomerization of intramolecularly hydrogen-bonded indigoid switches is severely disrupted.[18–23] A clear mechanistic framework to explain this observation has not been established, yet we believe this to be crucial for the design and improvement of photochemical proton pumps. In related structures, the inhibition of photoisomerization has been attributed either to structural stabilization of one isomer or to

the possibility of excited-state intramolecular proton transfer (ESIPT, Scheme 1). Such an ESIPT can mediate the decay of the excited state back to the original ground state, without changing the configuration of the double bond. This has been convincingly demonstrated for indigo through both computational and experimental methods.[24–26] In addition, the group of Laraia used CASPT2/CASSCF calculations to support that ESIPT is a possible pathway for an indole-derived hemithioindigo.[19] We thus set out to explore the ESIPT hypothesis in the context of *N*-heterocyclic hemi-indigo dyes, as mechanistic insight can be used to improve future designs of protonation-gated switches

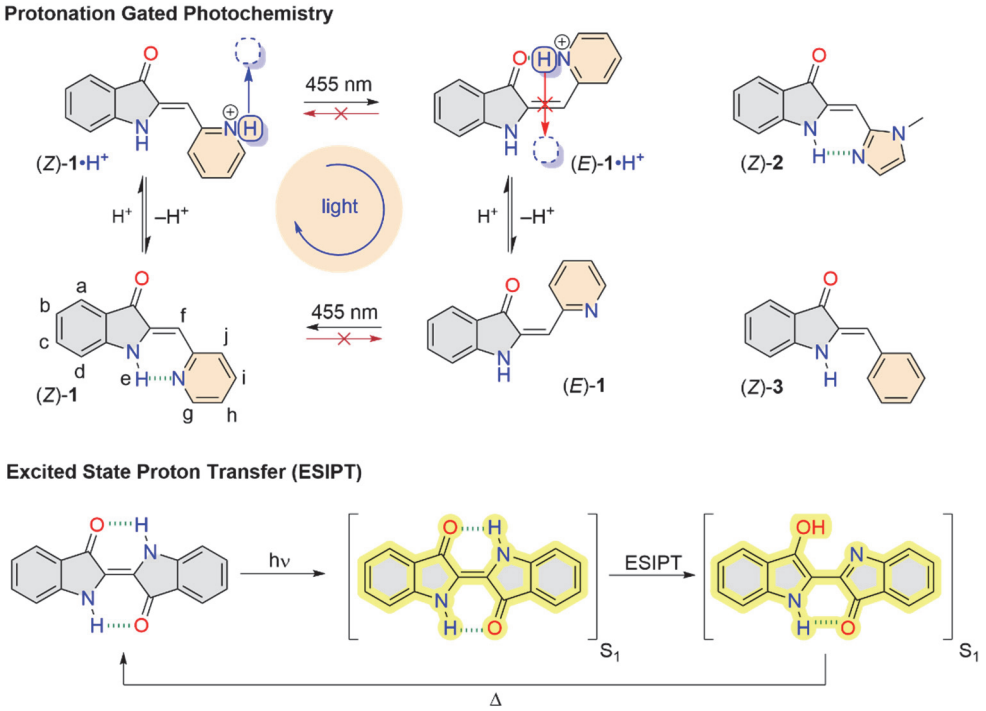

Scheme 1. (top) Protonation-gated photochemistry of hemi-indigo dyes **1**-**2** and reference compound **3**. (bottom) Excited state proton transfer (ESIPT) as a competitive decay channel in indigo blue.

Herein, we provide a mechanistic basis for the protonation-controlled photochemistry of hemi-indigo uncovered in Chapter 2, focusing on two representative switches, namely the pyridyl and imidazole derivatives (in this chapter (*Z*)-**1** and (*Z*)-**2**, respectively, see Scheme 1). As we hypothesize that ESIPT may be involved in the rapid de-activation of the excited state, we set out to characterize the excited-state lifetimes. In order to do so, we decided to combine steady-state spectroscopy with transient absorption spectroscopy (TA) and time-correlated single photon counting (TCSPC). Importantly, we demonstrate sizeable N-H/N-

D isotope effects on the excited-state lifetimes of the neutral *Z*-isomers, providing strong experimental evidence for a de-excitation mechanism involving the N-H/D vibrational mode. Using computational methods, namely TD-DFT and QM/MM, we provide further insight into the competition between proton/hydrogen-transfer and photoisomerization that governs the photochemistry of hydrogen-bonded hemi-indigo dyes.

3.2 Thermal and Photochemical Behavior

Where previous studies were performed in chloroform (Chapter 2), we here first studied the isomerization behavior in acetonitrile, as this solvent is preferred for the envisioned transient absorption spectroscopy experiments. It is known that halogenated solvents undergo photodecomposition under light irradiation[27], and are thus incompatible with the high laser intensity typically used in transient absorption spectroscopy. Thermal isomerization of (*Z*)-**1** and (*Z*)-**2** was monitored by ^{1}H NMR spectroscopy in acetonitrile in the presence and absence of trifluoroacetic acid (TFA, 32 equiv.). In the presence of TFA, a new set of signals corresponding to the protonated *E*-isomer appeared over the course of several days, characterized by the hydrogen-bonded NH signals at δ = 16.92 and 14.45 ppm (for **1** and **2**, respectively, Figure E1-E2), while without TFA no spectral changes were noted over a period of 3 weeks. Protonation thus induced thermal *Z*-to-*E* isomerization, and the rate of this process was determined by fitting the change in concentration of the *Z*-isomer to a first-order decay (half-lives ~ 3 d and 10 d for **1** and **2**, see Figure E3). The longer half-lives mark a clear increase in stability with respect to the studies performed in chloroform (Chapter 2).

The photochromic behavior of **1** was then probed using steady-state UV-Vis spectroscopy in acetonitrile. Irradiation of a solution of (*Z*)-**1** (75 μM, CH_3CN) with 405 nm, 455 nm, 525 nm, or 545 nm gave no observable changes in absorbance. Subsequently, aliquots of TFA were added, which resulted in the gradual redshift of the absorption spectrum of (*Z*)-**1** (λ_{max} = 480 to 485 nm, Figure 1), indicative of protonation. This redshift in absorption was less pronounced than in chloroform (λ_{max} = 482 to 504 nm, Chapter 2). The spectral changes were fitted to a 1:1 model using BindFit[28] to afford an equilibrium constant of $K = 3.0 \times 10^2$ M^{-1}. In further studies, excess TFA was used to ensure quantitative protonation. Irradiation of the protonated *Z*-isomer at 455 nm resulted in a redshift of the absorption maximum (λ_{max} = 533 nm, Figure 2) accompanied by a decrease in intensity, indicative of *Z*-to-*E* photoisomerization. Throughout irradiation, an isosbestic point was maintained at λ_{max} = 517 nm, characteristic of a unimolecular isomerization process.

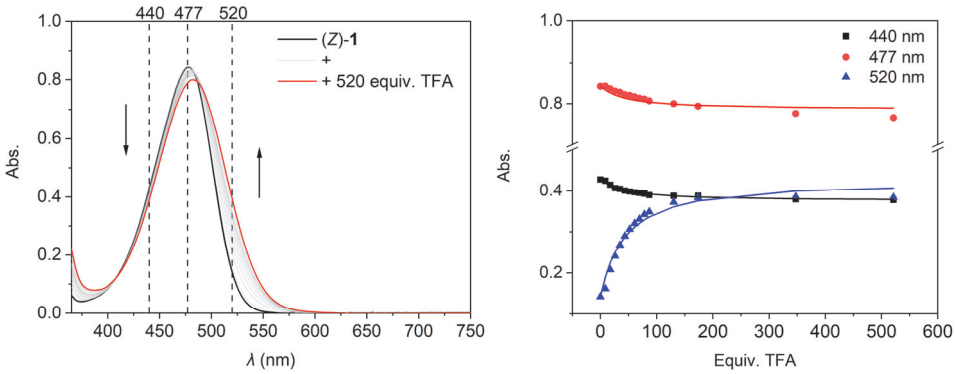

Figure 1. (left) UV-Vis spectral changes of (*Z*)-**1** (75 μM in degassed CH_3CN, 293 K), upon titration with TFA (1.3 M in CH_3CN) in a 1 cm cuvette. (right) Experimental absorbance values and data fitting (line) obtained by simultaneous analysis of absorbance at 440 nm, 477 nm, and 520 nm by Bindfit to a 1:1 model; $K = 3.0 \times 10^2\ M^{-1}$. This experiment was performed within 1 h, and thermal isomerization of (*Z*)-**1**·H^+ to (*E*)-**1**·H^+ is negligible on this experimental timescale

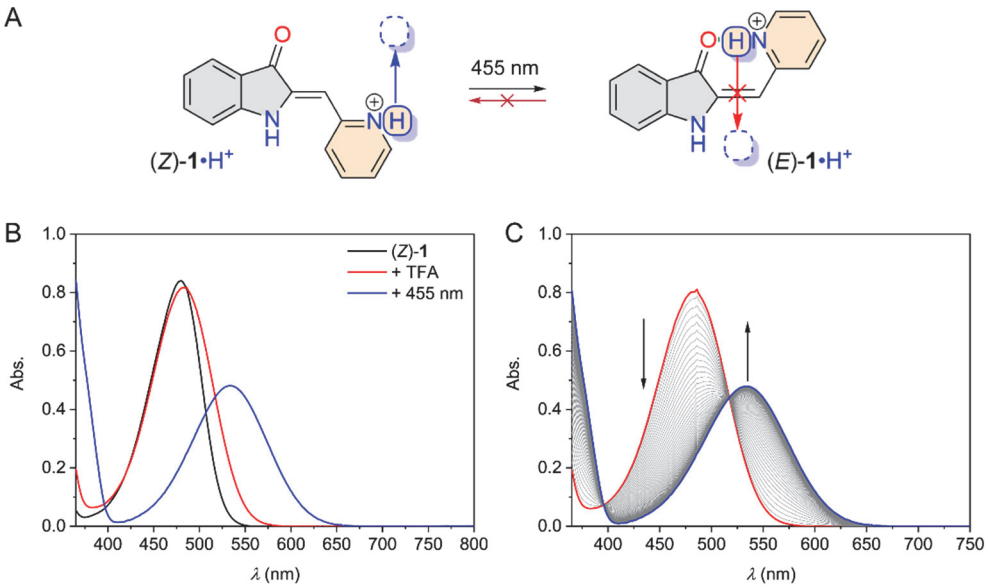

Figure 2. (A) Photoisomerization of (*Z*)-**1**·H^+ to (*E*)-**1**·H^+**.** (B) UV-Vis spectra starting with (*Z*)-**1** (75 μM in degassed CH_3CN, 273 K), addition of TFA (4.7×10^2 equiv.), and subsequent irradiation with 455 nm. (C) UV-Vis spectral changes upon photoisomerization of (*Z*)-**1**·H^+ (75 μM in degassed CH_3CN, 273 K, 4.7×10^2 equiv. TFA) by irradiation with 455 nm light (60 s interval). A clear isosbestic point is maintained at $\lambda = 517$ nm.

The photogenerated *E*-isomer was subjected to irradiation at various wavelengths between 405 nm and 660 nm (405 nm, 455 nm, 525 nm, 591 nm, 640 nm, and 660 nm), and no spectral changes were observed, even when irradiating at wavelengths where only the *E*-isomer absorbed.

Deprotonation with Et_3N resulted in a blueshift of the absorption maximum (λ_{max}= 533 to 486 nm, Figure 3), and irradiation with 455 nm light now did result in clear spectral changes, namely an increase in absorbance and a blueshift of the absorption maximum, characteristic of the reverse *E*-to-*Z* photoisomerization.

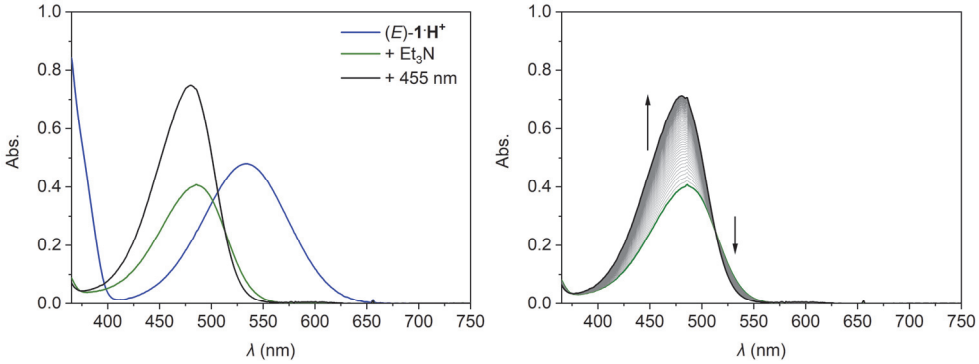

Figure 3. (left) UV-Vis spectra of (*E*)-**1**·H^+ (75 μM in degassed CH_3CN, 273 K, formed by 455 nm irradiation at a concentration of 75 μM in the presence of 4.7×10^2 eq TFA), addition of Et_3N (7.0×10^2 equiv.), and subsequent irradiation with 455 nm. (right) UV-Vis spectral changes upon photoisomerization of (*E*)-**1** (75 μM in degassed CH_3CN, 273 K, 4.7×10^2 equiv. TFA and 7.0×10^2 equiv. Et_3N) by irradiation with 455 nm light (100 s interval). A clear isosbestic point is maintained at λ = 513 nm.

The UV-Vis data and spectral changes upon irradiation for imidazole hemi-indigo derivative **2** were analogous to **1** and matched those reported in our previous work.[17] That is, in the protonated state, only *Z*-to-*E* photoisomerization takes place, while the neutral compound isomerizes only from the *E*-isomer to the *Z*-isomer. The only key difference observed is that (*Z*)-**2** blueshifted upon protonation (λ_{max} = 485 to 468 nm), in contrast to (*Z*)-**1**, this difference was also noted in our previous studies in chloroform (Chapter 2). The spectral profiles of **2** are shown in Figure 4 (kinetic traces in Figure E4).

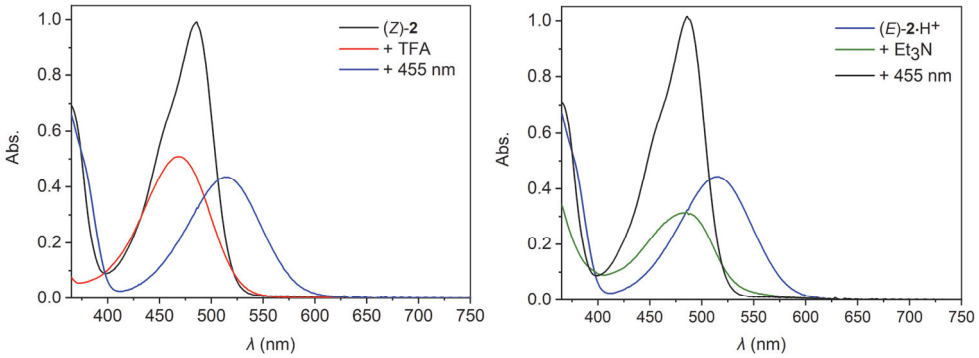

Figure 4. (left) UV-Vis spectra starting with (*Z*)-**2** (70 μM in degassed CH_3CN, 273 K), addition of TFA (4.7×10^2 equiv.), and subsequent irradiation with 455 nm. (right) UV-Vis spectra of (*E*)-**2**·H^+ (70 μM in degassed CH_3CN, 273 K, 4.7×10^2 eq TFA), addition of Et_3N (7.0×10^2 equiv.), and subsequent irradiation with 455 nm.

Photochemical *Z*-to-*E* isomerization in the protonated state was additionally followed by ^1H NMR spectroscopy. Addition of TFA to (*Z*)-**1** resulted in the downfield shift of most NMR signals, most notably those corresponding to the pyridyl ring (Hj, Hi, Hh, and Hg, see Figure 5). Upon irradiation with 455 nm light, the signals corresponding to the *Z*-isomer disappeared, while a new set of signals appeared that could be assigned to the *E*-isomer. By relative signal integration, it was confirmed that quantitative *Z*-to-*E* isomerization occurred upon irradiation of the protonated *Z*-isomer with 455 nm light (Figure 5 and Figure E5). An identical experiment was performed for **2**, and also in that case, quantitative photoconversion was observed upon irradiation with 455 nm light (Figures E6-E7).

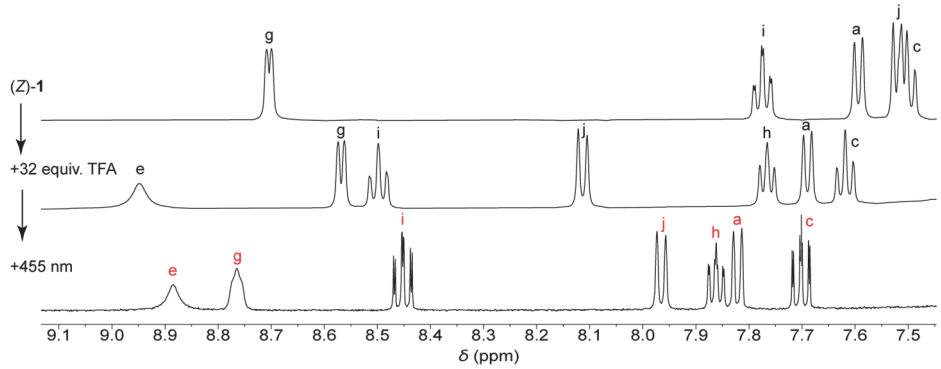

Figure 5. ^1H NMR (500 MHz, CD_3CN) spectra following addition of TFA (32 equiv.) to (*Z*)-**1** (5.7 mM) and quantitative photoisomerization to the *E*-isomer upon irradiation with 455 nm light. See Scheme 1 for proton assignment. See Figure E5 for additional spectra.

The quantum yields of photoisomerization were subsequently determined in acetonitrile using a ferrioxalate actinometer, following a reported procedure (Table 1 and Figures E8-E10).[17] By monitoring the UV-Vis spectral changes of concentrated solutions of the protonated *Z*-isomer or the neutral *E*-isomer upon irradiation with 455 nm light, the rates of formation of the respective photoisomer could be quantified. By comparing this to the known photon flux, determined using the ferrioxalate actinometer, the quantum yields were calculated. The values obtained are similar to those previously reported in chloroform (Chapter 2), except that the quantum yield for the *Z*-to-*E* photoreaction of **2**·H^+ is higher in acetonitrile (1.1% versus 0.2% in chloroform).

Table 1. Photoisomerization quantum yields of hemi-indigos **1**-**2**.[a]

HI	$\Phi_{Z\cdot H^+ \rightarrow E\cdot H^+}$ (%)	$\Phi_{E \rightarrow Z}$ (%)
1	0.53 (3.0×10^{-4})	0.38 (9.5×10^{-3})
2	1.10 (0.12×10^{-2})	3.90 (8.0×10^{-1})[b]

[a]At 455 nm irradiation in CH_3CN at 273 K, unless otherwise noted. [b] Determined at 263 K.

3.3 Transient Absorption Spectroscopy

We then studied the photophysical properties of **1** with transient absorption spectroscopy. This entails populating the excited-state with a femtosecond excitation laser pulse (pump) followed by a broad white-light pulse (probe). Unlike steady-state UV-Vis spectroscopy, which quantifies the electronic transitions of the ground state, this method is used to probe the spectral properties of the molecule in the excited state. A molecule in the excited-state can absorb an additional photon (*i.e.,* transitioning from S_1 to S_{1+n}), and is characterized by a specific UV-Vis absorption profile, referred to as the excited-state absorption (ESA). Since the excited state is not generated quantitatively, the optical properties of the excited state are inferred from the differential absorption spectrum (ΔAbs), which is determined by Equation 1. That is, the pure ground-state absorption as obtained by probing the sample before the laser excitation is subtracted from the absorption spectrum obtained at a defined time interval (*t*) after the laser pump pulse (Eq. 1).

$$\Delta Abs = A_t - A_0 \qquad \text{(Eq. 1)}$$

The ESA is thus characterized by a positive ΔAbs signal, whereas ground-state bleaching (GSB) or stimulated emission (SE) is measured as a negative ΔAbs signal. By changing the delay between the pump and probe pulse, a time-dependent profile of the excited state is obtained with ~0.1 ps resolution. The resulting dataset, referred to as the transient matrix,

contains the intensity of ΔAbs versus wavelength and delay time. After outlier removal and baseline correction, this matrix can be fitted through global analysis[29] to reveal the decay kinetics. In addition to providing lifetimes of the different components in a (sequential) kinetic model, global analysis also provides the evolution-associated spectra (EAS). These EAS represent the spectral profile associated with a specific time constant. While EAS are mathematical constructs and not equivalent to pure ESA, they provide a meaningful tool for identifying key spectral changes associated with each kinetic component.

The transient absorption of (*Z*)-**1** was studied upon excitation at 455 nm. A positive ESA was found between 450 and 600 nm at early times, but the spectral shape redshifted slightly during the first few picoseconds, characterized by a rising component at 560 nm. The ESA initially masks the GSB, but at later times, the GSB was observed below 480 nm, which matched with the spectral profile of the ground-state absorption of (*Z*)-**1** (λ_{max} = 480, Figure 1 and 6). Global analysis using Glotaran[30] of the transient absorption matrix revealed that the spectral evolution is well described by a sequential three-exponential decay model (Figure 7).

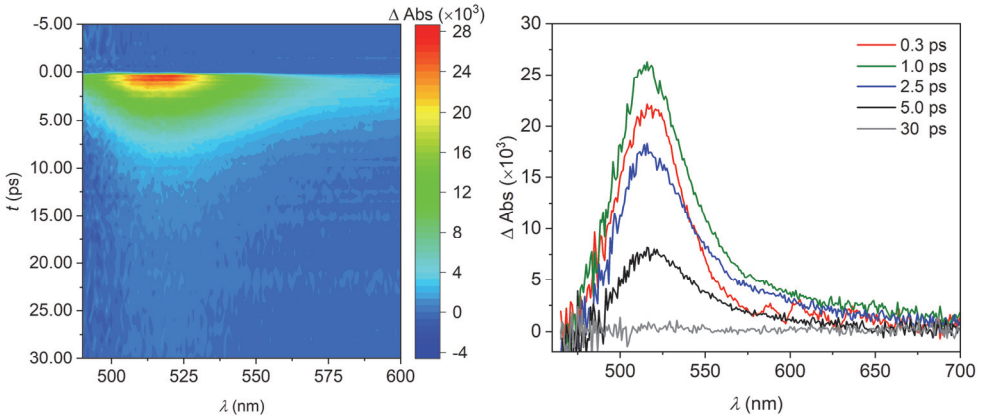

Figure 6. (left) 3D plot of ΔAbs versus time and wavelength with excitation at 450 nm on (*Z*)-**1** (350 μM, in degassed and dry CH_3CN). (right) Representative spectra capturing the decay of the excited-state population.

The first evolution-associated spectrum corresponds to a short-lived component that decays within ~ 1 ps into a species with a broader absorption profile (Figure 7). We attribute this to vibrational cooling of the S_1 Franck Condon (FC) state and concomitant solvent relaxation to a local minimum on the S_1 PES. This short-lived component in turn evolved to form an intermediate species on a ~ 3 ps timescale, possibly a (proton-transferred) tautomer. Finally, this intermediate decayed with a lifetime of ~ 13 ps to the original ground-state spectrum. We hypothesized that if ESIPT indeed occurs, we might capture this by probing the excited-

state lifetimes of the deuterated species; *i.e.,* whether there is a H/D kinetic isotope effect.[31,32] We argued that in the presence of 1 v% D_2O the N-H proton could be exchanged *in situ*, which was confirmed by separate ^{1}H- and ^{2}D-NMR experiments (Figure E11). Importantly, upon repeating the experiments in the presence of 1 v% H_2O, similar lifetimes are observed as in neat, dry CH_3CN, yet addition of 1 v% D_2O resulted in an elongation of the excited-state lifetime, yielding a strong isotope effect (Figure 8 and Figure E12, Table 1, $\tau_2 = 5.29$, $\tau_D/\tau_H = 1.9$). This pronounced isotope effect confirms that the N-H/N-D vibrational mode is involved in the de-excitation, which is in agreement with an excited-state proton transfer.

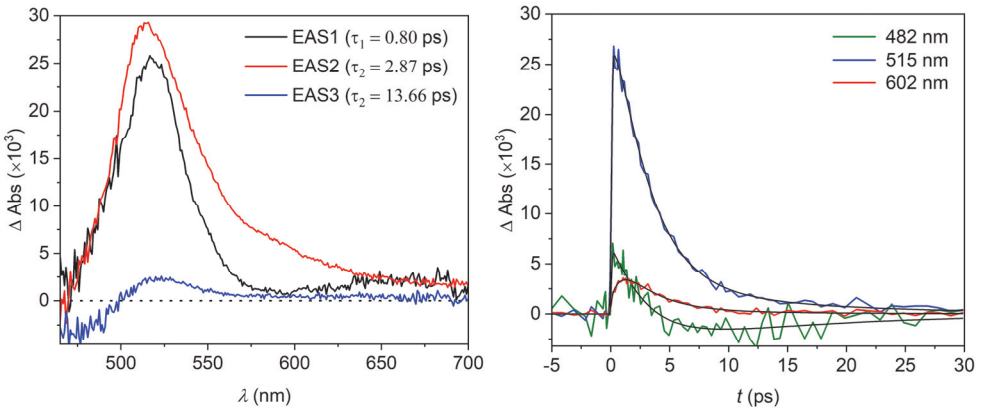

Figure 7. (left) Representative evolution associated spectra (EAS) and their associated time constants of (*Z*)-**1**. (right) Kinetic traces with the fit (black line) as obtained by global analysis of the whole transient data matrix of (*Z*)-**1**.

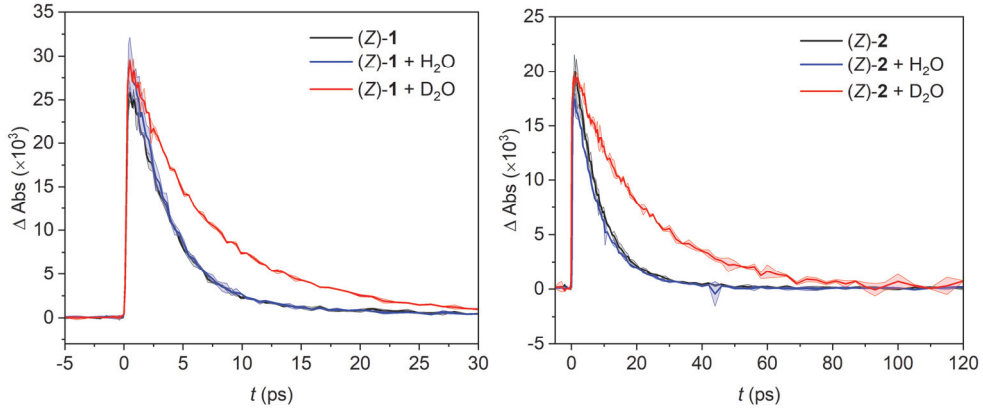

Figure 8. Transient absorption (averaged over λ = 515 – 525 nm) to probe the effect of the addition of either 1 v% H_2O or D_2O on the excited-state lifetime. Standard deviation of duplicate measurements shown. (left) (*Z*)-**1** (350 μM, CH_3CN) (right) (*Z*)-**2** (300 μM, CH_3CN).

We then explored the effect of protonation (to disrupt the intramolecular hydrogen bonding) on the transient absorption of (*Z*)-**1**. In the presence of TFA the transient absorption of (*Z*)-**1**·H$^+$ is much longer-lived. ESA was observed around 450 to 600 nm, while negative absorption was found centered around ~ 680 nm. This negative signal was assigned to SE, as GSB could be ruled out based on the mismatch with the GS absorbance of (*Z*)-**1**·H$^+$ (λ_{max} = 485).

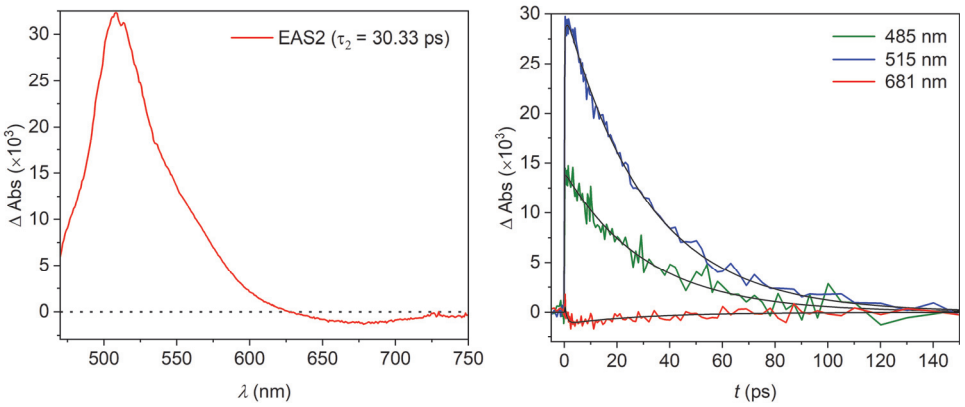

Figure 9. (left) Representative evolution associated spectrum (EAS) and its associated time constants of (*Z*)-**1** + TFA. EAS1 not plotted, as it is dominated by the coherent artefact (Figure E14). (right) Kinetic traces with the fit (black line) as obtained by global analysis of the whole transient data matrix of (*Z*)-**1** + TFA.

In this case, the transient data matrix was best described by a biexponential decay (Figure 9), with one fast and one long-lived component. The fast component (EAS1, Figure E14) is attributed to vibrational cooling (~ 1 ps), and the slower one (EAS2, Figure 9) to relaxation back to the ground state (~ 30 ps). Importantly, protonation using TFA-d_1 had no significant effect on the excited-state lifetimes (Table 2, Figure E13).

Subsequently, samples of (*E*)-**1**·H$^+$ were prepared by photoisomerization of solutions of (*Z*)-**1** with 455 nm light in the presence of TFA. Transient absorption could be measured after tuning the excitation laser to 580 nm. Two transient absorption maxima were observed, centered around ~ 485 nm and ~ 640 nm. The transient data were fitted through global analysis to a three-component exponential decay, with lifetimes in the order of 1, 4, and 14 ps (Figure 10). A clear dip in the absorption spectra of all three components is observed above 530 nm, which could be assigned to the GSB of (*E*)-**1**·H$^+$ (λ_{max} = 533). Analogous to (*Z*)-**1**, the three components could represent excitation to a vibrationally hot excited state, which relaxes to a local minimum before evolving to a longer-lived intermediate with blue-shifted absorption. Unlike (*Z*)-**1**, protonation with TFA-d_1 to give the deuterated intramolecularly

hydrogen-bonded *E*-isomer, did not result in a significant isotope effect on any of the lifetimes (Figure E15, Table 2).

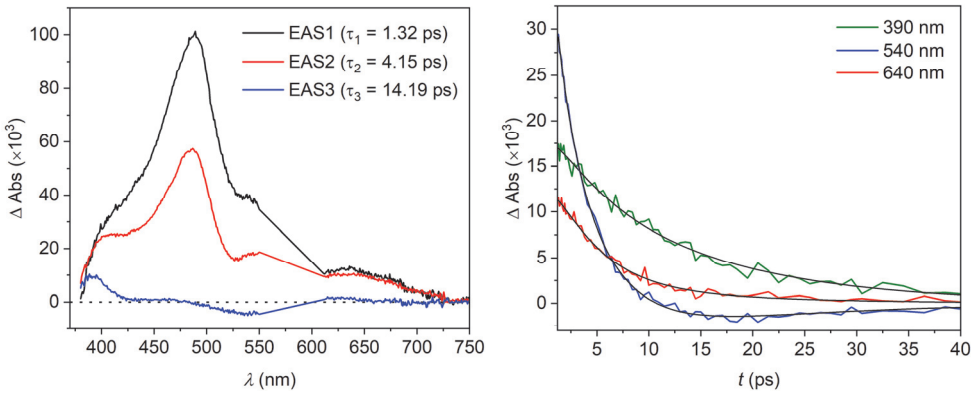

Figure 10. (left) Representative evolution associated spectra (EAS) and their associated time constants of (*E*)-**1** + TFA. (right) Kinetic traces with the fit (black line) as obtained by global analysis of the whole transient data matrix of (*E*)-**1** + TFA.

The kinetic parameters obtained, all as averages of two separate experiments, have been summarized in Table 2. In general, two different sequential kinetic models provided satisfactory fits of the transient data matrix, containing either two or three components.

Table 2. Excited-state lifetimes of **1** obtained after global analysis of transient data matrix and fitting to a sequential kinetic model. The standard deviation is shown of two independent samples.

HI	Additive	τ_1 (ps)	τ_2 (ps)	τ_3 (ps)
(*Z*)-**1**	-	0.76 (0.10)	2.87 (0.02)	13.66 (0.20)
(*Z*)-**1**	+ H_2O	0.68 (0.03)	2.79 (0.12)	12.38 (1.33)
(*Z*)-**1**	+ D_2O	0.60 (0.02)	5.21 (0.41)	13.57 (0.48)
(*Z*)-**1**	+ TFA	0.76 (0.09)	30.33 (0.63)	-
(*Z*)-**1**	+ TFA-d_1	1.65 (0.71)	32.24 (0.04)	-
(*E*)-**1**	+ TFA	1.32 (0.14)	4.15 (0.14)	14.19 (0.01)
(*E*)-**1**	+ TFA-d_1	1.22 (0.15)	4.62 (0.03)	13.74 (0.15)

We then moved to the imidazole derivative **2**, where we found that although the lifetimes are somewhat longer, the general trend is comparable to **1** (Table 3). That is, the decay of (*Z*)-**2**

after excitation could only be accurately described with a three-component sequential kinetic model. Again, a sizeable kinetic isotope effect was obtained when comparing the transient kinetics in the presence of 1 v% H_2O to that in the presence of 1 v% D_2O (Figure 8). The photoactive, protonated *Z*-isomer is significantly longer-lived, and stimulated emission was observed around 605 nm. The protonated *E*-isomer is again shorter-lived, with more complex kinetics following a three-component exponential decay pathway. The transient absorption spectra (Figures E16-E18) and the corresponding evolution associated spectra (Figures E19-E21) are comparable to those observed for **1**.

Table 3. Excited-state lifetimes of **2** obtained after global analysis of transient data matrix and fitting to a sequential kinetic model. The standard deviation is shown of two independent samples.

HI	Additive	τ_1 (ps)	τ_2 (ps)	τ_3 (ps)
(*Z*)-**2**	-	0.49 (0.06)	6.50 (0.04)	12.93 (1.44)
(*Z*)-**2**	+ H_2O	0.50 (0.03)	7.06 (0.28)	12.32 (0.05)
(*Z*)-**2**	+ D_2O	0.42 (0.00)	7.55 (0.29)	23.60 (0.26)
(*Z*)-**2**	+ TFA	0.97 (0.08)	83.12 (0.57)	
(*Z*)-**2**	+ TFA-d_1	0.81 (0.07)	82.12 (1.57)	
(*E*)-**2**	+ TFA	0.94 (0.12)	9.21 (0.59)	17.85 (1.06)
(*E*)-**2**	+ TFA-d_1	0.95 (0.01)	8.00 (0.42)	16.51 (0.80)

3.4 Fluorescence and TCSPC

The stimulated emission observed in the transient spectra of the protonated *Z*-isomers led us to examine the fluorescence properties of **1** and **2**. Steady state fluorescence emission was first measured for (*Z*)-**1** in acetonitrile. This revealed a weak, but measurable fluorescence signal centered around λ_{em} = 554 nm, with the excitation scan profile matching the absorption spectrum of (*Z*)-**1** (Figure 11). After the addition of TFA, the fluorescence intensity increased, and an emission peak was observed at λ_{em} = 625 nm, in agreement with the stimulated emission profile found in the transient absorption experiments (Figure 11). A qualitative comparison revealed the fluorescence quantum yields to be much lower than that of $Ru(bpy)_3$ ($\Phi_{fluo} < 0.1\%$).

Similarly, a weak fluorescent emission was found for (*Z*)-**2** (λ_{em} = 546 nm) and a significantly stronger and redshifted fluorescence signal was observed for (*Z*)-**2**·H^+ (λ_{em} = 605 nm), in

agreement with the observed stimulated emission in the transient absorption experiments (Figures E22-E23). The lifetimes of (*Z*)-**1**·H^+ and (*Z*)-**2**·H^+ were additionally quantified using TCSPC (Figure E24). The decay of the fluorescent signal could be fitted to a single exponential decay in both cases, and the obtained lifetimes are in excellent agreement with those obtained from the global analysis of the transient absorption data. The fluorescence of (*Z*)-**1** and (*Z*)-**2** was too weak to obtain TCSPC traces of sufficient quality.

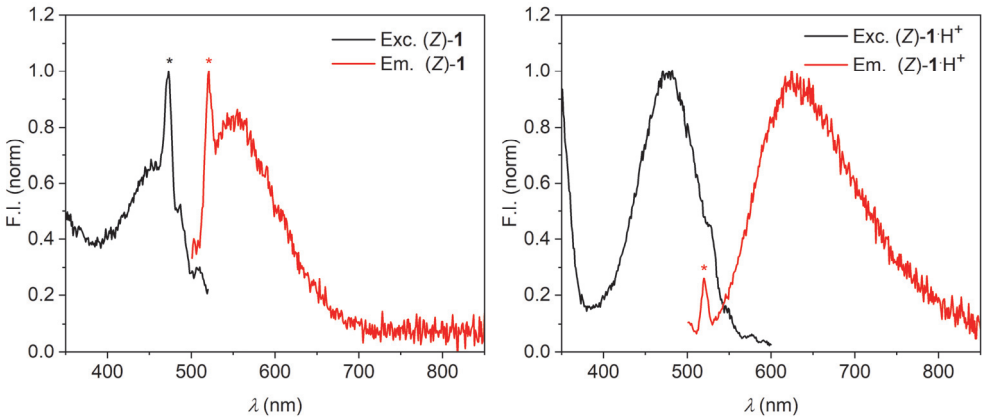

Figure 11. (left) Normalized excitation (λ_{em} = 550 nm, 8.9 μM (*Z*)-**1**) and emission (λ_{exc} = 450 nm, 27 μM (*Z*)-**1**) spectra in CH_3CN. (right) Normalized excitation (λ_{em} = 630 nm, 8.9 μM (*Z*)-**1**) and emission (λ_{exc} = 450 nm, 27 μM (*Z*)-**1**) spectra in CH_3CN. Peaks marked with * are due to Raman scattering.

Table 4. Fluorescence lifetimes of **1**-**3** as determined by fitting of TCSPC data, reported with standard deviation of repeated experiments on unique samples.

HI	Additive	τ_{fl}
(*Z*)-**1**	+ TFA	31.3 (1.2×10^{-5}) ps
(*Z*)-**2**	+ TFA	88.5 (3.4×10^{-4}) ps
(*Z*)-**3**	-	3.91 (4.0×10^{-3}) ns
(*Z*)-**3**	+ H_2O	1.70 (2.0×10^{-2}) ns
(*Z*)-**3**	+ D_2O	1.995 (7.0×10^{-3}) ns

Finally, in order to validate the isotope effect on the lifetime of the *Z*-isomers, we decided to compare the effect of deuteration on parent phenyl hemi-indigo (*Z*)-**3** using TCSPC. First of all, the parent, non-hydrogen-bonded hemi-indigo **3** has a lifetime in the ns regime, three orders of magnitude longer lived than (*Z*)-**1**. The fluorescence lifetime is halved upon

addition of water (1 v%), and a minor isotope effect is observed upon addition of D_2O (Figure E25), far smaller than observed in the case of (*Z*)-**1** and (*Z*)-**2**. The decrease in fluorescence lifetime of hemi-indigo **3** upon complexation with water has been previously reported, with a tentative explanation proposed based on solvent-solute hydrogen bonding reducing the S_0 and S_1 energy gap and thus increasing the efficiency of internal conversion.[33]

3.5 Quantum Chemical Calculations

The large isotope effect observed in the transient absorption of (*Z*)-**1** establishes the involvement of the N-H or N-D vibrational mode in the de-excitation pathway. Furthermore, the three-component sequential model observed for (*Z*)-**1** and (*E*)-**1**·H^+ is compatible with the formation of a proton-transferred species as a transient intermediate.

We sought to test this hypothesis by performing (TD)-DFT calculations ((CAM)-B3LYP/6-311++G(d,p) with an IEFPCM CH_3CN solvent model, Table E1). A relaxed scan along the N-H distance of (*Z*)-**1** on the S_0 surface revealed that formation of the PT tautomeric species (*Z*)-**1**T is highly unfavorable (Figure 12). In contrast, on the S_1 surface the ESIPT tautomer (*Z*)-**1**T is thermodynamically favored. Comparison of single point S_0 energies at the S_1 geometry across the N-H bond scan demonstrates that the S_0-S_1 energy gap narrows upon tautomerization. This suggests that fluorescence from (*Z*)-**1**T would be highly redshifted, around 763 nm (Table E2). Experimentally, we did not observe such redshifted emission, likely because (Z)-**1**T is not emissive or too short-lived. It should be noted that also in transient spectroscopy experiments on the related indigo, no SE band could be assigned to the enol form.[20]

The intermediate observed with TA spectroscopy might alternatively correspond to the ground-state (*Z*)-**1**T, which decays on the S_0 PES to reform (*Z*)-**1**. However, (TD)-DFT calculations of the proton transfer transition state energies on both the S_0 and S_1 surfaces exclude this possibility (Figure 12). On the S_1 PES, ESIPT is associated with a small barrier of only 0.08 eV (1.8 kcal/mol), corresponding to a lifetime of approximately 3.5 ps, which agrees well with the experimentally observed lifetime τ_2 of 2.8 ps. Note that in this analysis the proton transfer occurs on a single excited-state surface. In case ESIPT is directly associated with a conical intersection that mediates decay to S_0, this computational approach is no longer valid. The back tautomerization on the S_0 reaction pathway, on the other hand, is virtually barrierless (0.04 eV or 0.84 kcal/mol). Previous studies on (*Z*)-**1** by Ikegami *et al.* also support the presence of a small proton transfer barrier on the S_1 PES, as they observed no fluorescence in ethanol at room temperature, but upon cooling to 77 K detected emission at 520 nm with an 8 ns lifetime.[23] Thus, we argue that most likely after excitation of (*Z*)-**1** to the FC state, vibrational relaxation leads to an S_1 minimum that undergoes ESIPT to form the

excited-state tautomer. This process has a small barrier, which is prone to a sizable isotope effect. The timescales of the decay resemble those observed for indigo[20], and for indigo carmine[26] where a similar isotope effect of 1.5 (τ_D/τ_H) was found. Likely, a nearby conical intersection facilitates non-radiative de-excitation from (*Z*)-**1**T, with a barrierless tautomerization recovering (*Z*)-**1** on the ground-state. Similarly, for indigo CASSCF/CASPT2 calculations suggested that a (single) proton transfer on the S_1 surface forms a mono-enol minimum, from which a conical intersection is reached through an additional in-plane deformation.[25]

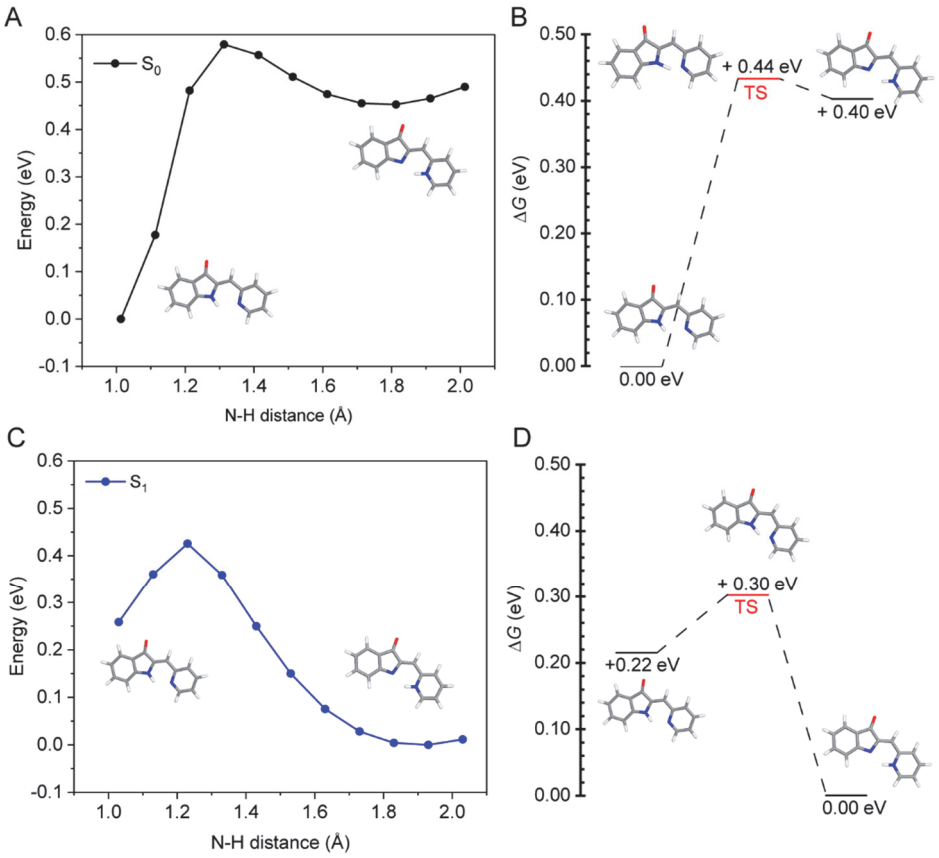

Figure 12. (A) Relaxed scan along the N-H distance of (*Z*)-**1** on the S_0 PES (B3LYP/6-311++G(d,p)). (B) Energy minimized geometry of the two tautomeric local minima and the associated transition state on the S_0 PES alongside their relative Gibbs free energies (B3LYP/6-311++G(d,p)). (C) Relaxed scan along the N-H distance of (*Z*)-**1** on the S_1 PES (CAM-B3LYP/6-311++G(d,p)). (D) Energy minimized geometry of the two tautomeric local minima and the associated transition state on the S_1 PES alongside their relative Gibbs free energies (CAM-B3LYP/6-311++G(d,p)).

Computational data on ground state and excited-state tautomerization of (*Z*)-**2** is in line with that observed for (*Z*)-**1** (Figures E27-E29), with the exception that on the S_1 PES of (*Z*)-**2** a somewhat higher barrier is found for proton transfer. This is in agreement with the longer lifetime found in the TA setup. An analogous computational analysis of (*E*)-**1**·H^+ with (TD)-DFT indicated that proton transfer is an energetically uphill process both on the S_0 and the S_1 PES (Figure E26), and based on these preliminary calculations, ESIPT appears an unlikely mechanism for the protonated *E*-isomer.

(TD)-DFT is unable to describe non-adiabatic crossings between the S_0 and the S_1 PES. To obtain a more realistic picture of the excited-state surface, in particular of the protonated species, we moved to state-of-the-art QM/MM calculations to identify relevant conical intersections (Figure 13 for QM/MM-model, Experimental Section for details). First, absorption bands were computed using SA3-CASPT2/6-31G* (12e,11o) level of theory, which were in reasonable agreement with the experimental spectra (Figure E30 and Table E3). After confirming that this model could accurately describe the protonated species' absorption profile, conical intersection geometry optimizations were performed using CASSCF, after which single-point energy corrections were performed on the CASPT2 level of theory.

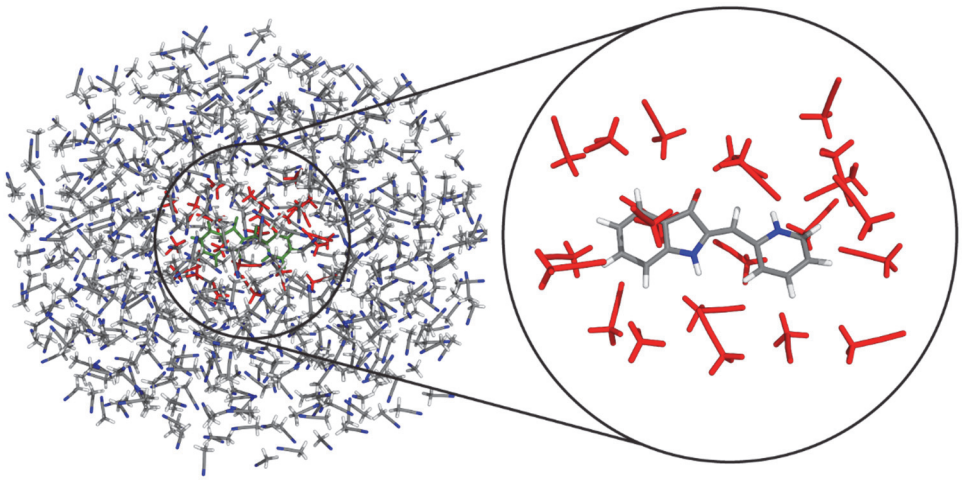

Figure 13. Construction of the QM/MM model to be used for computing vertical excitation energies and the S_1 photodynamics in MeCN solvent environment**.** (left) The entire model, including the frozen solvent sphere (H = white, C = grey, N = blue), the mobile MM-treated CH_3CN solvent molecules (red), and the QM-treated hemi-indigo in green. (right) The flexible QM/MM model with the QM (*Z*)-**1**·H^+ (H = white, C = grey, N = blue, O = red) and the MM CH_3CN molecules (red).

Exploration of the S_1 PES of (*Z*)-**1**·H^+ revealed a local S_1 minimum (53.0 kcal/mol) close to the Franck Condon (FC) region (78.4 kcal/mol), accessible by vibrational relaxation after vertical excitation (Figure 14). The fluorescence of the S_{1min} is computationally predicted to be λ_{em} = 670 nm (CAS-SCF/RMS-CASPT/6-31G*), in good agreement with the TA and fluorescence data (λ_{em} = 625 nm). Interestingly, a near-conical intersection (NearCoIn) was found close to this S_{1min}, which is in fact lower in energy. The structural reorganization associated with this pathway is typical of double-bond isomerization, as a dihedral angle (N–C=C–C(Pyr)) of 99.2° was found (Figure 14). However, the true conical intersection associated with this NearCoIn lies at a higher energy (24.9 kcal/mol above the NearCoIn). In addition, the CoIn is highly sloped, which is typically associated with unfavorable branching ratios towards the photoproduct, and is thus predictive of a low quantum yield.[34] Nevertheless, we can conclude that a photoisomerization decay channel is accessible for (*Z*)-**1**·H^+. Importantly, we did not explore the trajectory between S_{1min} and the NearCoIn itself, which would be necessary to predict the decay timescale. Overall, the S_1 PES is compatible with our assignment of the TA data; fast relaxation from the S_1 FC state to the S_{1min} (< 1 ps) populates the fluorescent S_{1min}, which then decays through the NearCoIn decay region (30 ps).

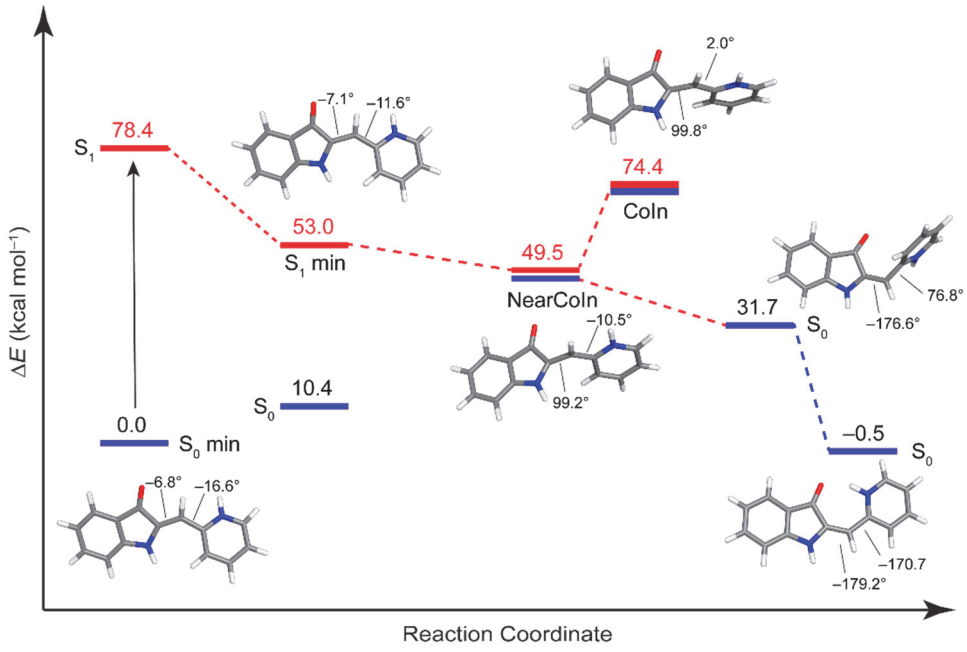

Figure 14. Key species on the S_1 potential energy surface of (*Z*)-**1**·H^+ as determined by CASSCF//CASPT2/6-31G*. Energies with respect to the S_0 minimum of (*Z*)-**1**·H^+. Double bond dihedral angle taken as (H)N–C=C–C(Pyr), single bond dihedral as H–C–C–N(Pyr).

Analysis of the S_1 PES of the excited-state surface of (*E*)-**1**·H$^+$ revealed more complex features, and three different conical intersections were identified. Each CoIn mediates a unique process, namely internal conversion, photoisomerization, and hydrogen-atom transfer (Figure 15). After vertical excitation, a local S_{1min} (45.8 kcal/mol) is within reach through vibrational relaxation. From this local minimum three different pathways are feasible.

An unusual CoIn at 65.2 kcal/mol was found following a stretching deformation; the structure is almost fully planar with no torsional component. Its presence hints at an ultrafast de-excitation channel that enables fast non-radiative decay. However, the CoIn is energetically uphill from the S_{1min} (19.4 kcal/mol higher in energy). Importantly, no such CoIn was found for (*Z*)-**1**·H$^+$. A NearCoIn is found at 59.8 kcal/mol, with significant rotation around the double bond (dihedral angle N–C=C–C(Pyr) of 95.4°), typical of double-bond isomerization. However, the actual conical intersection is energetically highly unfavorable (114.6 kcal/mol), and topographically extremely sloped, predictive of an undetectable quantum efficiency for photoisomerization. This is a clear qualitative difference with (*Z*)-**1**·H$^+$; for (*E*)-**1**·H$^+$ the NearCoIn associated with photoisomerization lies above the S_{1min}, and second of all the CoIn associated with the decay region is even more sloped than was the case for (*Z*)-**1**·H$^+$. This is fully compatible with the lack of photoisomerization observed experimentally, as the decay region essentially acts as an internal conversion channel given the expected quantitative branching ratio back to the ground state of (*E*)-**1**·H$^+$.[34] The calculations thus suggest that photoisomerization of (*Z*)-**1**·H$^+$ is more feasible than for (*E*)-**1**·H$^+$. Lastly, similar in energy to the NearCoIn, at 59.8 kcal/mol, a CoIn is found that is associated with H-transfer from the pyridinium N-H to the carbonyl, which is best described as a hydrogen-atom transfer rather than the anticipated proton transfer. Notably, pyramidalization of the olefin C-H is observed at the CoIn with respect to the S_{1min}. The conical intersection is predicted to be effective, as it is only marginally higher in energy than the S_{1min}.

The three-component exponential decay observed in (*E*)-**1**·H$^+$ with TA spectroscopy mirrors the profile observed for (*Z*)-**1** and supports the possibility of a proton/hydrogen-transferred intermediate. Although no clear isotope effect was identified for (*E*)-**1**·H$^+$, this does not exclude the possibility of proton/hydrogen transfer. In some cases where ESIPT was unambiguously identified experimentally, still no isotope effect was observed.[35,36] In particular, when the process is barrierless, any observed non-equilibrium isotope effect originates from differences in vibrational frequencies of X-H and X-D.[32] More detailed calculations on the hydrogen-atom transfer mechanism and the associated vibrational modes are ongoing at the CASSCF/CASPT2 level of theory to further elucidate these dynamics.

Importantly, the CoIn associated with HAT for (*E*)-**1**·H$^+$ is not solely based on the N-H vibrational mode, but also on pyramidalization of the olefinic C-H.

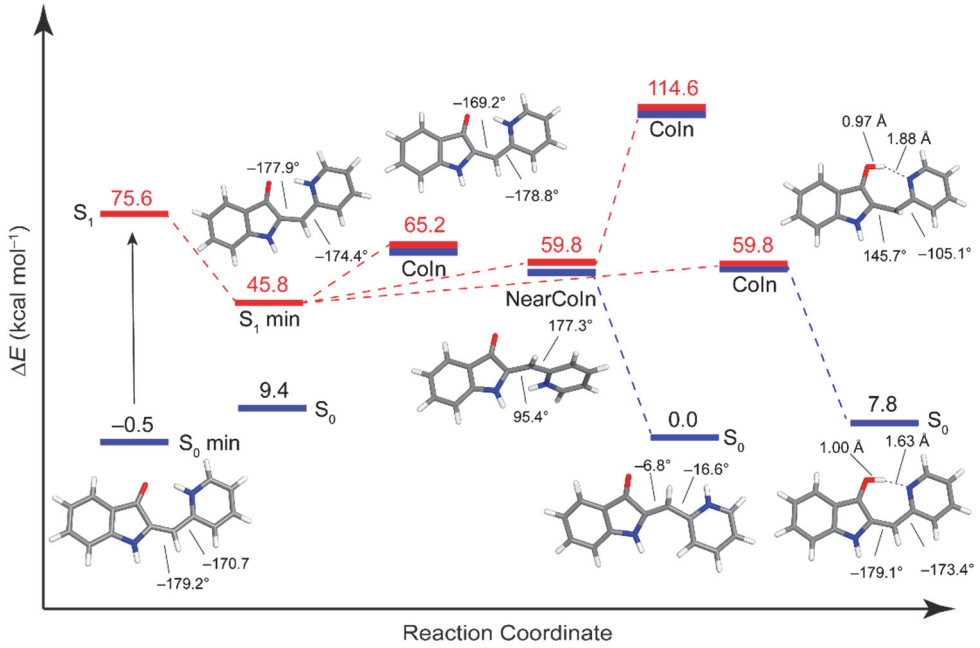

Figure 15. Key species on the S_1 potential energy surface of (*E*)-**1**·H$^+$ as determined by CASSCF//CASPT2/6-31G*. Energies with respect to the S_0 minimum of (*Z*)-**1**·H$^+$. Double bond dihedral angle taken as (H)N–C=C–C(Pyr), single bond dihedral as H–C–C–N(Pyr).

Multiple de-excitation channels are thus accessible on the S_1 PES of (*E*)-**1**·H$^+$, all contributing to the lack of photoisomerization of the hydrogen-bonded *E*-isomer. The computational data on (*E*)-**1**·H$^+$ are in line with the more complex decay kinetics observed with TA spectroscopy. The possibility of decaying through qualitatively different channels challenges the fully sequential kinetic model we have applied to the TA absorption data. To facilitate comparison with the experimental data, calculations of the excited-state emission and absorption profiles are underway.

3.6 Conclusion

In summary, we investigated the protonation-gated photophysical properties of *N*-heterocyclic hemi-indigo switches. In particular, we quantified the effect of protonation on the excited-state lifetimes using transient spectroscopy and TCSPC measurements, and determined the sensitivity of these lifetimes to H/D-isotope effects. The data reveals that the photochemistry of hydrogen-bonded heterocyclic hemi-indigo dyes is governed by a competition between a hydrogen/proton-transfer and photoisomerization. Pronounced

kinetic isotope effects on the excited-state lifetimes of (*Z*)-**1** and (*Z*)-**2** support that ESIPT suppresses productive photoisomerization, a conclusion supported by (TD)-DFT calculations. High-level QM/MM calculations further rationalize the difference between the protonated *Z*- and *E*-isomers. Although conical intersections associated with double-bond isomerization are identified in both cases, the CoIn found on the S_1 PES of (*E*)-**1**·H^+ is predicted to be extremely inefficient, while non-radiative decay and hydrogen atom transfer are operative as competitive de-excitation channels. The presence of an intramolecular hydrogen bond thus dictates photochemistry by providing additional unique decay channels.

Tracing the effect of non-covalent interactions on excited-state properties through transient absorption data and high-level QM/MM calculations advances our mechanistic understanding of how to direct excited-state pathways, which will aid the future design of chemically gated photoswitches.

3.7 Contributions

N. Duindam, S. J. Wezenberg, and A. M. Brouwer conceived the project. N. Duindam performed the steady state UV-Vis and NMR experiments and the (TD-)DFT calculations. N. Duindam and A. M. Brouwer performed the fluorescence spectroscopy, TA spectroscopy, and TCSPC measurements with technical support of M. Hilbers and W. Roeterdink. M. S. Bezabih and M. Olivucci performed the QM/MM calculations. S. J. Wezenberg, A. M. Brouwer, and M. Olivucci guided the project. N. Duindam acknowledges T. de Haas and D. Barreiro Lage for fruitful discussions regarding the (TD-)DFT calculations.

3.8 Experimental Section

General methods and materials

The degassing of the solvents was carried out by purging with N_2 for 15 min, unless noted otherwise. All commercially available chemicals were used without further purification. Compounds **1**, **2**, and **3** were synthesized as previously reported. ^{1}H and ^{13}C NMR spectra were recorded on Bruker AV 400, Bruker 500 Ultra Shield, and Bruker AV 600 instruments at 298 K unless indicated otherwise. CD_3CN was purchased from Eurisotop and used without further purification. Chemical shifts (δ) are denoted in parts per million (ppm) relative to residual protiated solvent (CD_3CN: for ^{1}H detection, δ = 1.94 ppm; for ^{13}C detection, δ = 1.32 ppm). The splitting pattern of peaks is designated as follows: s (singlet), d (doublet), t (triplet), q (quartet), p (quintet), h (septet), m (multiplet), br (broad). UV-Vis spectra were recorded on an Agilent Cary 8454 spectrometer using 1 cm or 1 mm quartz cuvettes and a Newport 20CGA-360 KI162 Longpass filter was placed in front of the light source of the spectrophotometer to absorb all incident light below 360 nm. Irradiation of UV-Vis and NMR samples was carried out using LEDs purchased from Thorlabs, i.e. mounted fiber-coupled LEDs M365F1 (3.0 mW), M385FP1 (18 mW), M405F1 (3.0 mW), M455F3 LEDs (17 mW), unmounted epoxy-encased LED465E (20 mW), LED525E (2.5 mW), LED591E (2 mW) and LED630E (7.2 mW), and an unmounted LED with glass lens LED660L (13 mW).

^{1}H NMR thermal isomerization studies

Solutions were prepared of the *Z*-isomer in CD_3CN to a final concentration of 5.7 mM. Samples with (32 equiv.) and without TFA were prepared, and the NMR tubes were flame-sealed to avoid solvent/TFA evaporation. The spectral changes were followed over time at room temperature.

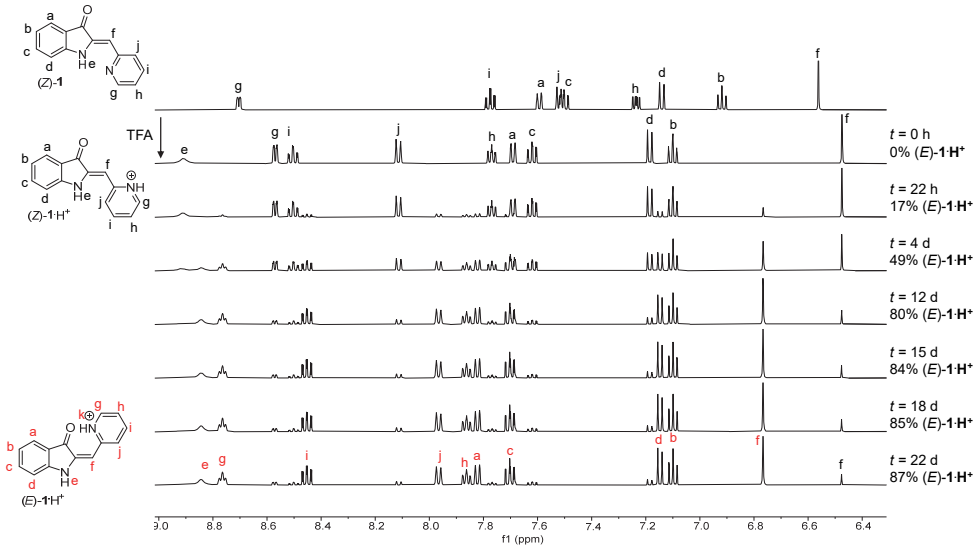

Figure E1. ^{1}H NMR spectral data (500 MHz, CD_3CN) following thermal equilibration of (*Z*)-**1** (5.7 mM) in presence of 32 equiv. TFA over time. The *E*/*Z*-ratio was obtained by integration of signals H**f** of (*E*)-**1**·H$^+$ and (*Z*)-**1**·H$^+$.

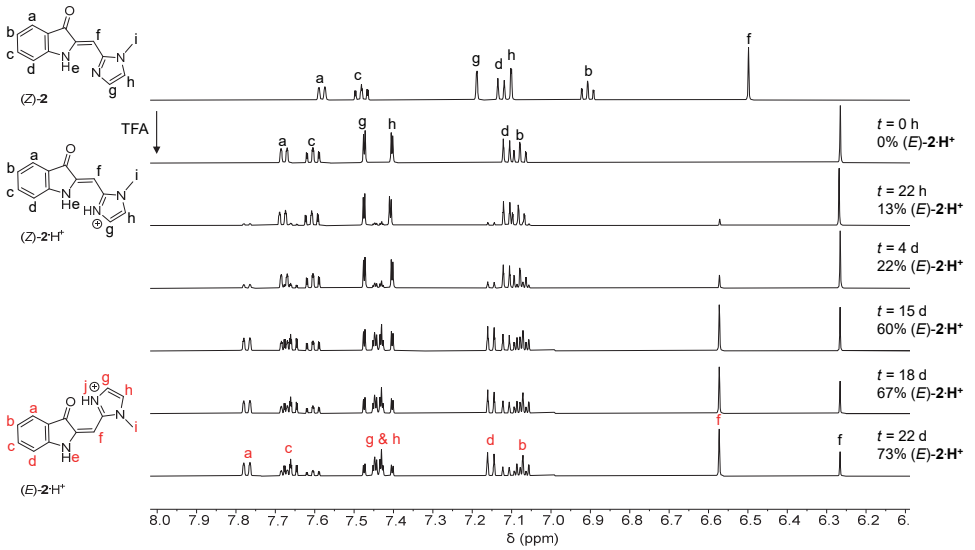

Figure E2. ^{1}H NMR spectral data (500 MHz, CD_3CN) following thermal equilibration of (*Z*)-**2** (5.7 mM) in the presence of 32 equiv. TFA over time. The *E*/*Z*-ratio was obtained by integration of signals H**f** of (*E*)-**2**·H$^+$ and (*Z*)-**2**·H$^+$.

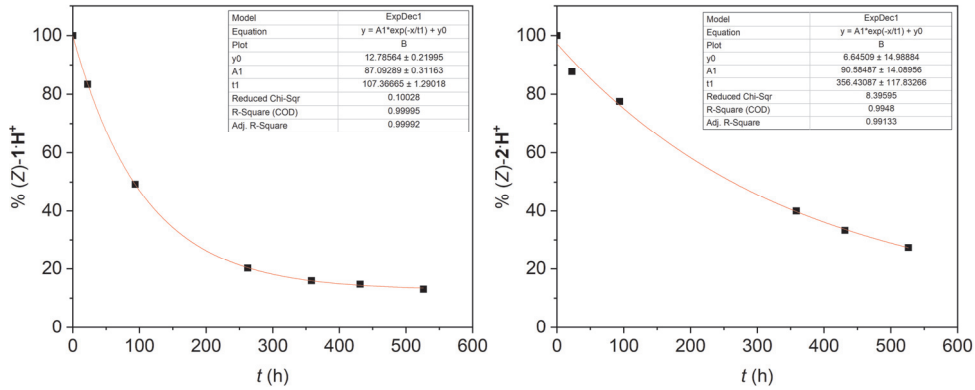

Figure E3. Fitting the percentage of (*Z*)-**1**·H$^+$ and (Z)-**2**·H$^+$ to a single exponential decay; $t_{1/2}$ = 74 h and 247 h, respectively (see Figures E1 and E2 for raw data).

UV-Vis Photoisomerization Studies

Solutions of the *Z*-isomers were prepared in dried and degassed spectroscopic grade acetonitrile at suitable concentrations (Abs < 1.0) in a 1 cm quartz cuvette. Samples of the *Z*-isomers were irradiated at 273 K with 405 nm, 455 nm, 465 nm, 525 nm for 300 s and the spectral changes were followed over time. After protonation with TFA (470 equiv.) photoisomerization upon irradiation with 455 nm was followed. The photogenerated *E*-isomer was subjected to irradiation with 405 nm, 455 nm, 525 nm, 591 nm, 640 nm, and 660 nm and the spectral changes were followed over time. After neutralization with Et_3N (700 equiv.), photoisomerization with 455 nm was followed at 263 K (for compound **2**) or 273 K (for compound **1**).

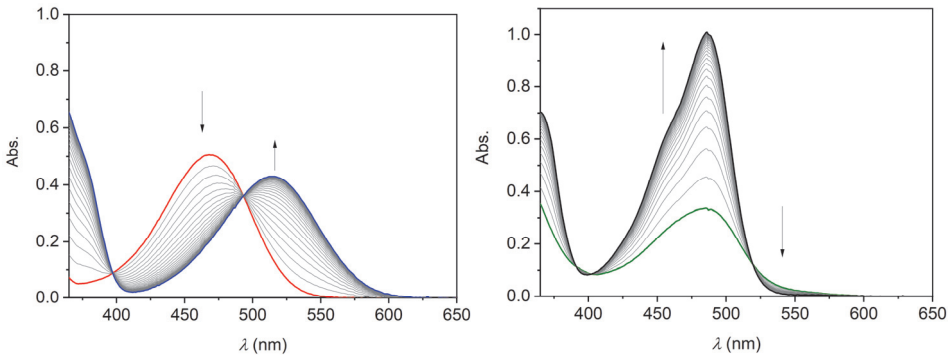

Figure E4. (left) UV-Vis spectral changes upon photoisomerization of (*Z*)-**2**·H^+ (70 μM in CH_3CN, 470 equiv. TFA, 273 K) by irradiation with 455 nm (60 s time interval). An isosbestic point is maintained at λ = 493 nm. (right) UV-Vis spectral changes upon photoisomerization of (*E*)-**2** (70 μM in CH_3CN, 470 equiv. TFA, 700 equiv. Et_3N, 263 K) by irradiation with 455 nm (10 s time interval). An isosbestic point is maintained at λ = 519 nm.

^{1}H NMR Photoisomerization Studies

Solutions of the *Z*-isomer were prepared in dried CD_3CN at a final concentration of 5.7 mM, and transferred to a J-Young tube to avoid solvent evaporation during photoirradiation.

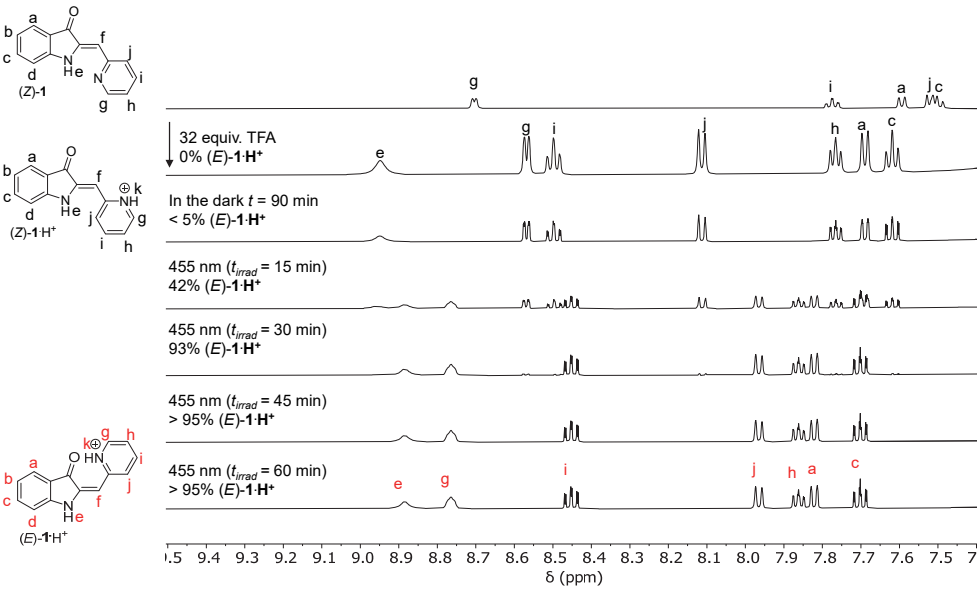

Figure E5. ^{1}H NMR (500 MHz, CD_3CN) spectra following quantitative photochemical conversion of (*Z*)-**1**·H$^+$ (5.7 mM) to (*E*)-**1**·H$^+$ upon irradiation with 455 nm light in the presence of excess TFA (trifluoroacetic acid, 32 equiv.). Prior to irradiation, the sample was kept in the dark for 90 minutes to confirm negligible thermal isomerization under the conditions used. The *E*/*Z*-ratio was obtained by integration of signals H**j** of (*E*)-**1**·H$^+$ and (*Z*)-**1**·H$^+$.

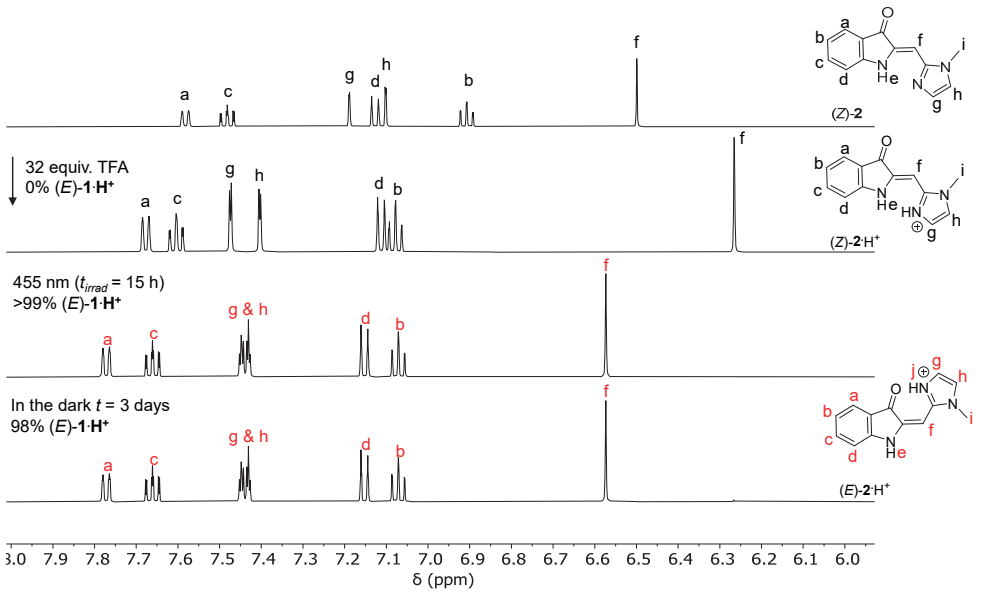

Figure E6. ^{1}H NMR (500 MHz, CD_3CN) spectra following quantitative photochemical conversion of (*Z*)-**2**·H$^+$ (5.7 mM) to (*E*)-**2**·H$^+$ upon irradiation with 455 nm light in the presence of excess TFA (trifluoroacetic acid, 32 equiv.). After irradiation, the sample was kept in the dark for 3 days to confirm that the quantitative conversion observed is solely due to photochemical isomerization. The *E*/*Z*-ratio was obtained by integration of signals H**i** of (*E*)-**2**·H$^+$ and (*Z*)-**2**·H$^+$.

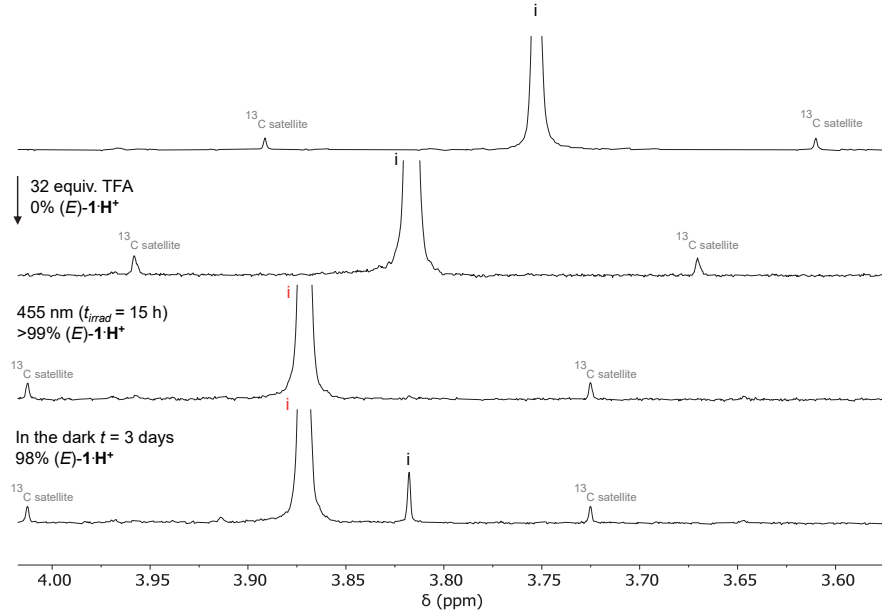

Figure E7. Amplified aliphatic region in the ^{1}H NMR spectrum shown in Figure E6.

Quantum Yield Determination

The photon flux of a Thorlabs M455F3 Fiber-coupled LED (λ_{max} = 455 nm) was determined at maximum power at 700 mA by measuring the production of ferrous ions from potassium ferrioxalate using a slightly adapted version of a previously published procedure.[37] Given the known quantum yield of ferrioxalate at the nearest known wavelength (ϕ = 1.09 at 457.9 nm)[38,39] the photon flux was determined to be 1.15×10^{-7} mol s^{-1}. For an elaborate description of the methodology, consult Chapter 2.

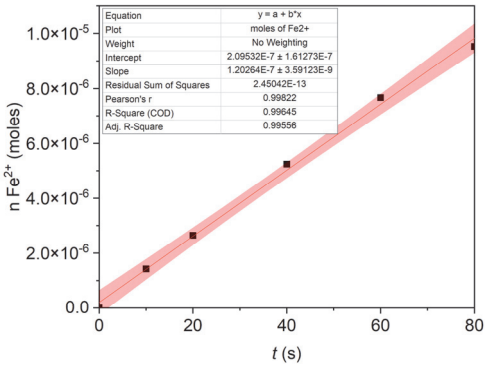

Figure E8. Moles of Fe^{2+} ions produced after irradiation of a 150 mM ferrioxalate solution (stirred at 1200 rpm in a 1 cm quartz cuvette, 293 K) at 455 nm and linear data fitting to determine the slope (95% confidence band visualized in red).

By following the photoisomerization of **1** and **2** in an identical irradiation set-up as the ferrioxalate irradiation, the quantum yield could be determined based on the rate of photoisomerization and the previously determined photon flux.

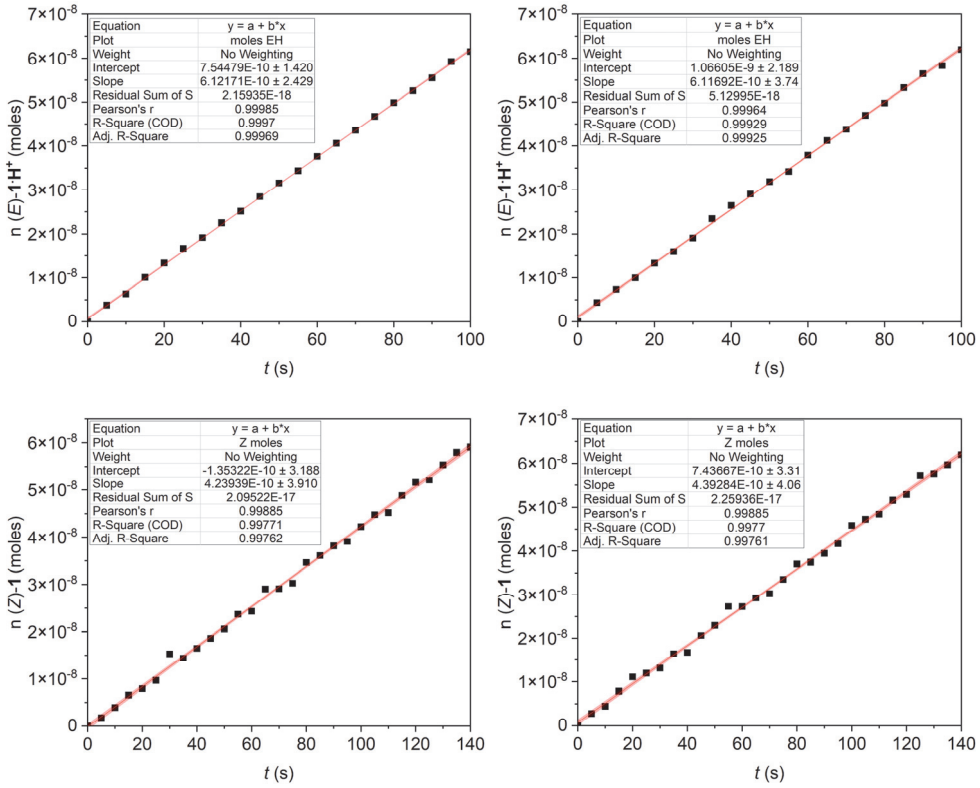

Figure E9. (top) Duplicate measurements of formation of (*E*)-**1**·H$^+$ upon irradiation of (*Z*)-**1**·H$^+$ (0.60 mM, 470 equiv. TFA) with 455 nm light. (bottom) Duplicate measurements of formation of (*Z*)-**1** upon irradiation of (*E*)-**1** (0.60 mM, 470 equiv. TFA neutralized with 700 equiv. Et_3N) with 455 nm light. (95% confidence band visualized in red).

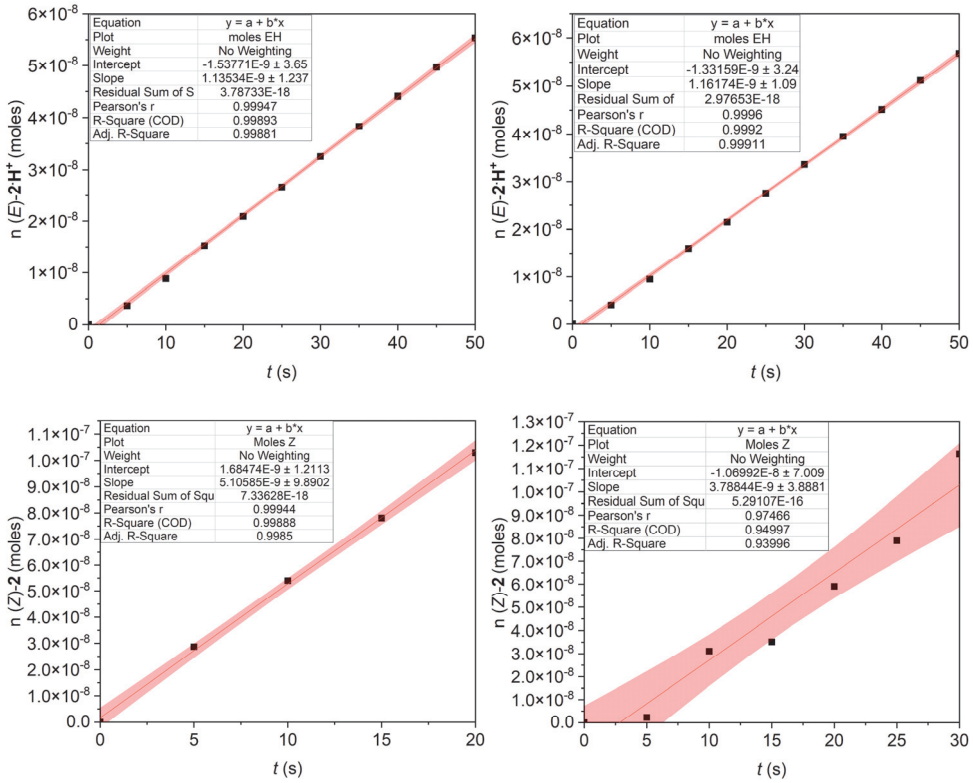

Figure E10. (top) Duplicate measurements of formation of (*E*)-**2**·H$^+$ upon irradiation of (*Z*)-**2**·H$^+$ (0.60 mM, 470 equiv. TFA) with 455 nm light. (bottom) Duplicate measurements of formation of (*Z*)-**2** upon irradiation of (*E*)-**2** (0.60 mM, 470 equiv. TFA neutralized with 700 equiv. Et_3N) with 455 nm light. (95% confidence band visualized in red).

^{1}H and ^{2}H NMR Deuterium Exchange Studies

To an NMR sample of (*Z*)-**1** (5.7 mM) was added in a sequential fashion 1 v% D_2O and 5 v% H_2O. The disappearance of the N-H signal and the appearance of the N-D signal (H**e**) was confirmed by ^{1}H NMR and ^{2}D NMR, respectively.

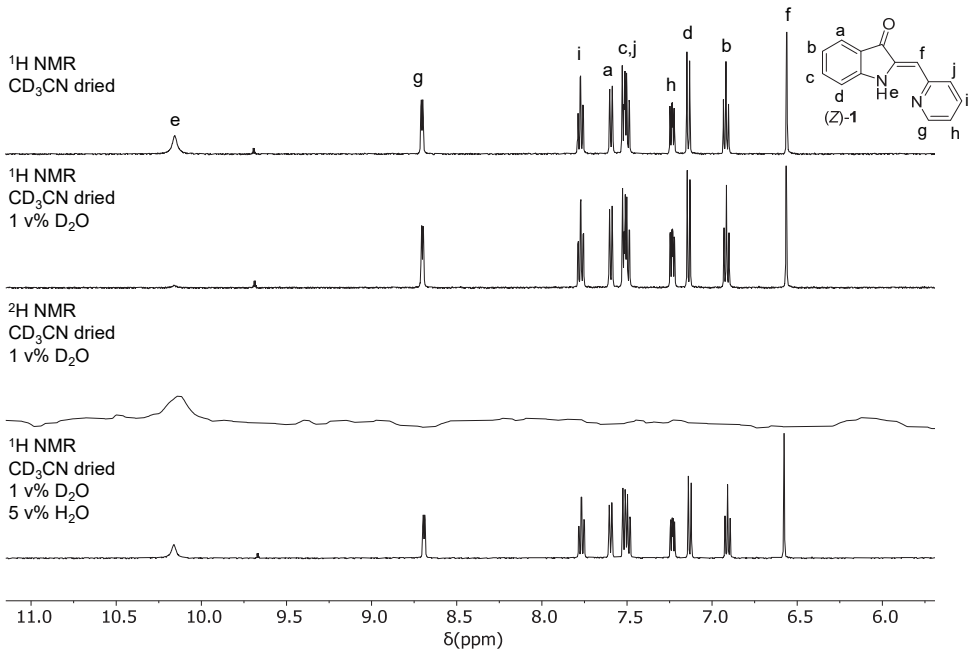

Figure E11. ^{1}H NMR (500 MHz, CD_3CN) and ^{2}D NMR (77 MHz, CD_3CN) of (*Z*)-**1** (5.7 mM) upon sequential addition of 1 v% of D_2O and 5 v% of H_2O.

Transient Absorption Spectroscopy

Transient absorption spectra were measured using a previously reported set-up.[40] A Ti:sapphire laser (Spectra Physics Solstice Ace) in conjunction with a OPA-C (Spectra-physics) was used to generate the white light probe beam and of the desired wavelength pump pulses (100 fs, 455 nm for the *Z*-isomers, 580 nm for the *E*-isomers). The beams were overlapped on a 2 mm cuvette, which was mounted on a movable stage and moved during the measurement to avoid excessive light exposure and subsequent photodecomposition.

Samples of the *Z*-isomers were prepared in dried and degassed CH_3CN, with concentrations such that such that the absorbance at the excitation wavelength (450 nm) ~ 0.5 in a 2 mm cuvette; 350 μM and 300 μM for **1** and **2**, respectively. UV-Vis spectra were measured before and after each transient absorption spectrum. UV-Vis spectra were measured before and after each transient absorption measurement. The *E*-isomers were photogenerated in the 1 mm quartz cuvette using 455 nm light in presence of TFA/TFA-d_1 (470 equiv.).

The transient data matrix was cleaned by removing outliers (both manually and by using the outlier detection on a 5 pixel window with a 3 pixel fence) and performing a baseline correction by subtraction of the first 6 timesteps as background using Glotaran 1.5.1.[29] Subsequently, global analysis was performed on the transient data matrix, fitting the data to a sequential kinetic model that includes the IRF, dispersion, and the coherent artefact. For (*E*)-**1** and (*E*)-**2** in the presence of TFA, the coherent artefact was so strong that a correct fit was only possible by removing the first 0.5 ps from the fitted region. The IRF and dispersion parameters were obtained from the whole timeframe and then treated as fixed parameters in the fitting of the dataset from 0.5 ps onwards.

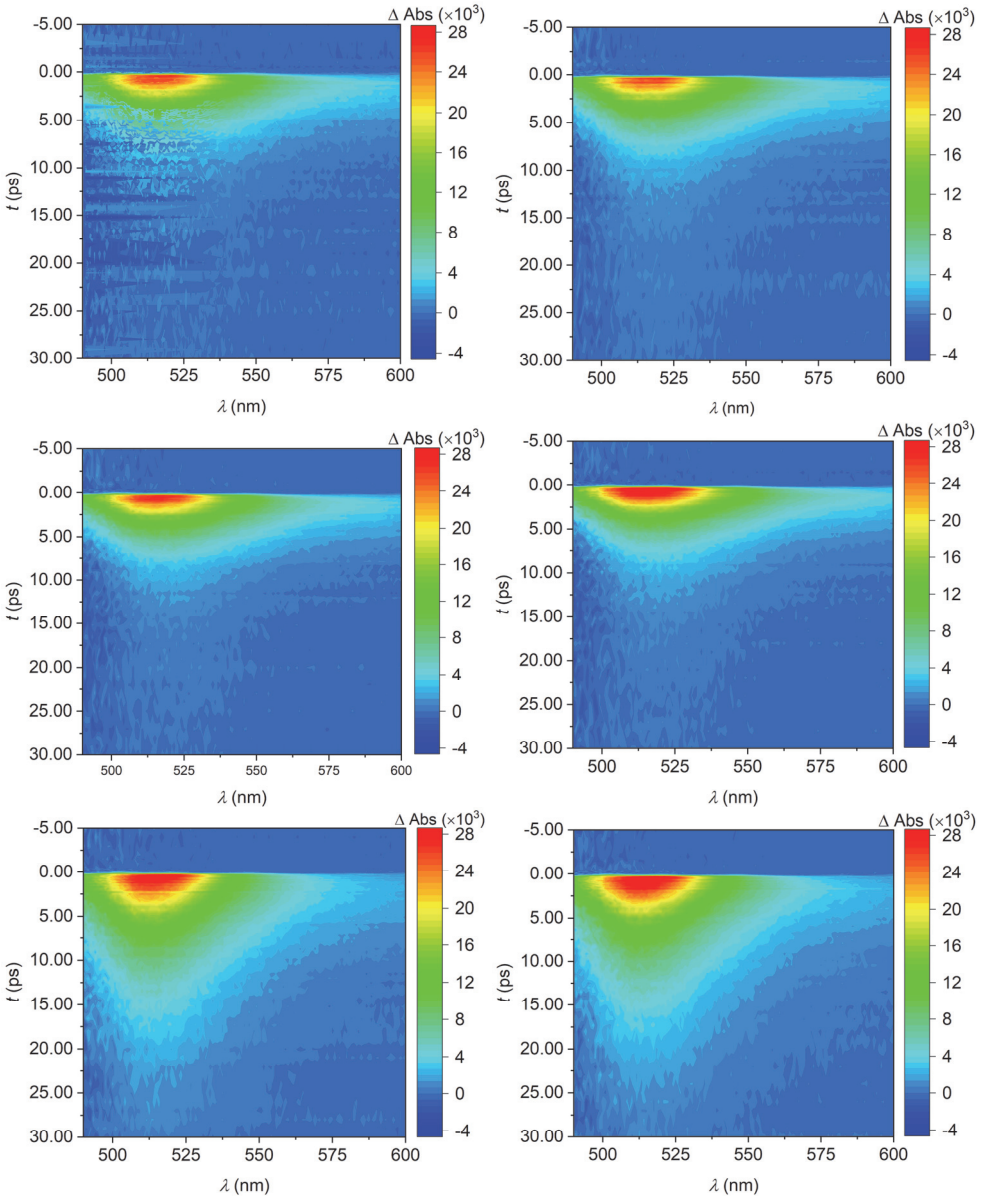

Figure E12. Duplicate transient absorption spectra obtained for (top) (*Z*)-**1**, (middle) (*Z*)-**1** + 1 v% H_2O, and (bottom) (*Z*)-**1** + 1 v% D_2O.

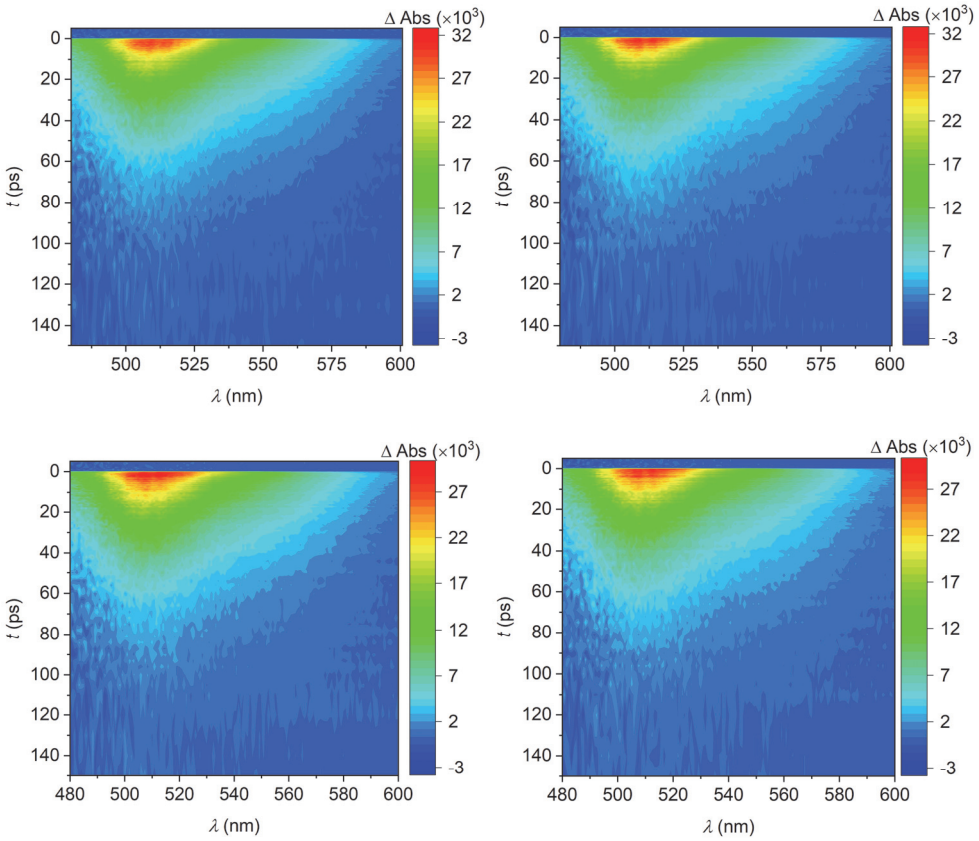

Figure E13. Duplicate transient absorption spectra obtained for (top) (*Z*)-**1** + TFA (470 equiv.), (bottom) (*Z*)-**1** + TFA-d_1 (470 equiv.).

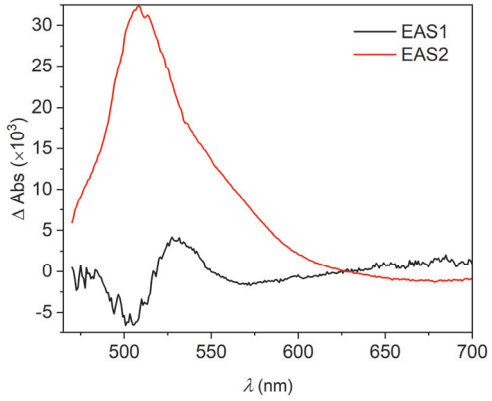

Figure E14. Representative evolution associated spectrum (EAS) and its associated time constants of (Z)-**1** + TFA.

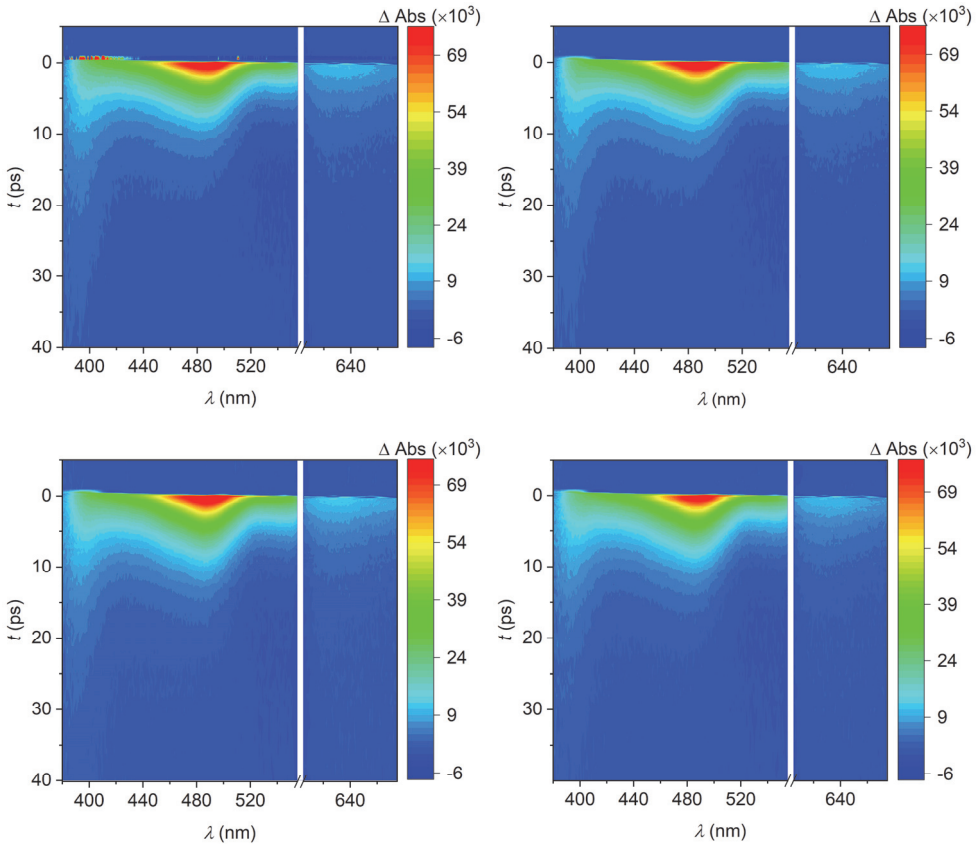

Figure E15. Duplicate transient absorption spectra obtained for (top) (*E*)-**1** + TFA(470 equiv.) and (bottom) (*E*)-**1** + TFA-d_1 (470 equiv.).

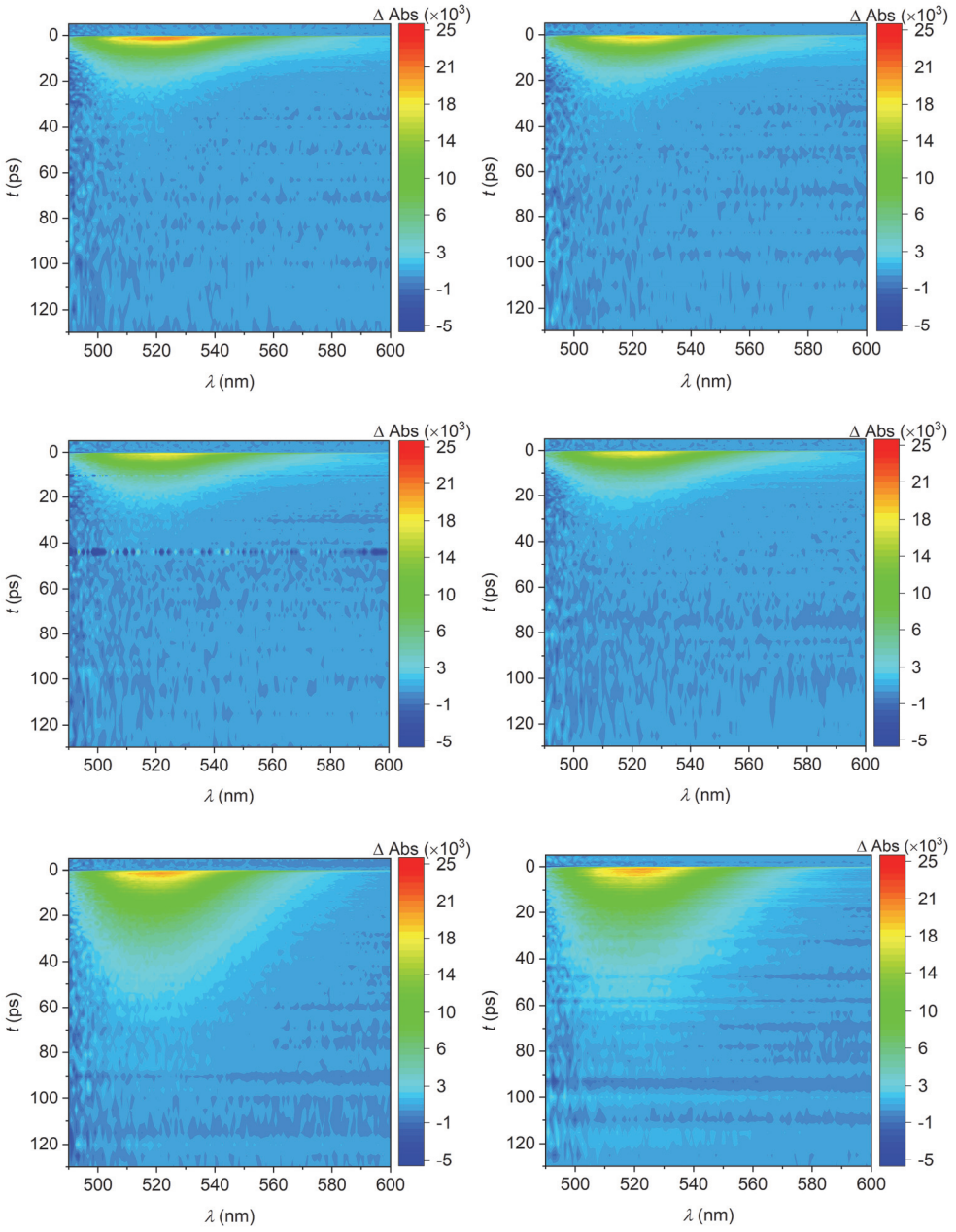

Figure E16. Duplicate transient absorption spectra obtained for (top) (*Z*)-**2**, (middle) (*Z*)-**2** + 1 v% H_2O, and (bottom) (*Z*)-**2** + 1 v% D_2O.

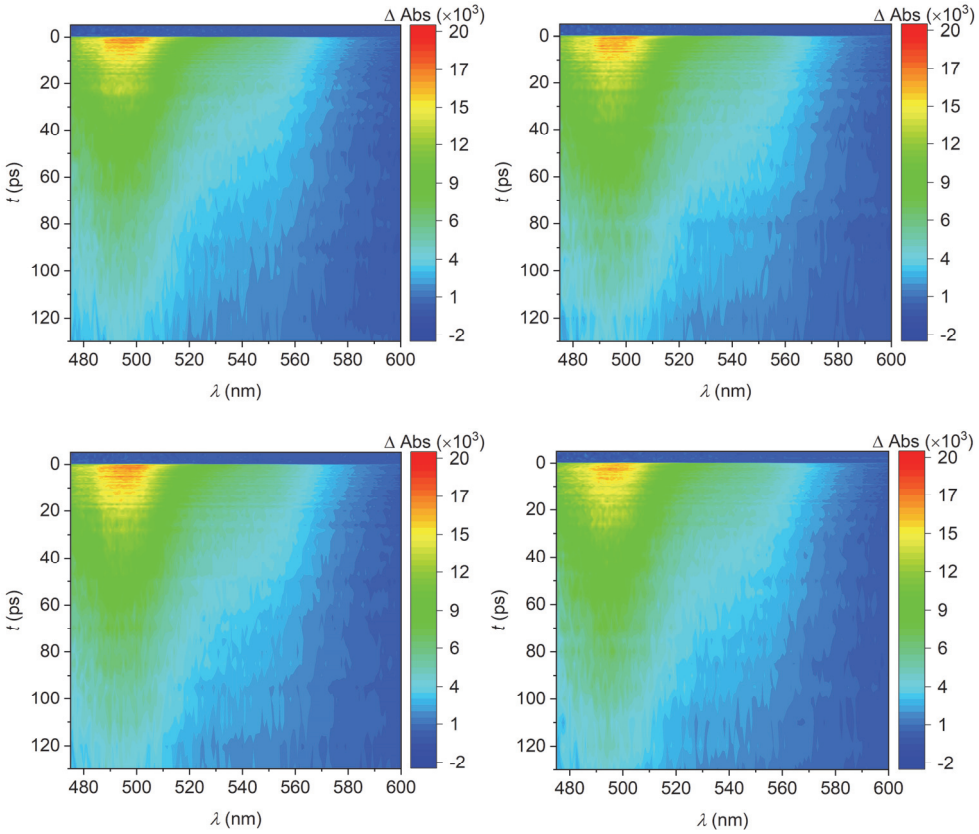

Figure E17. Duplicate transient absorption spectra obtained for (top) (Z)-**2** + TFA (470 equiv.), (bottom) (Z)-**2** + TFA-d_1 (470 equiv.).

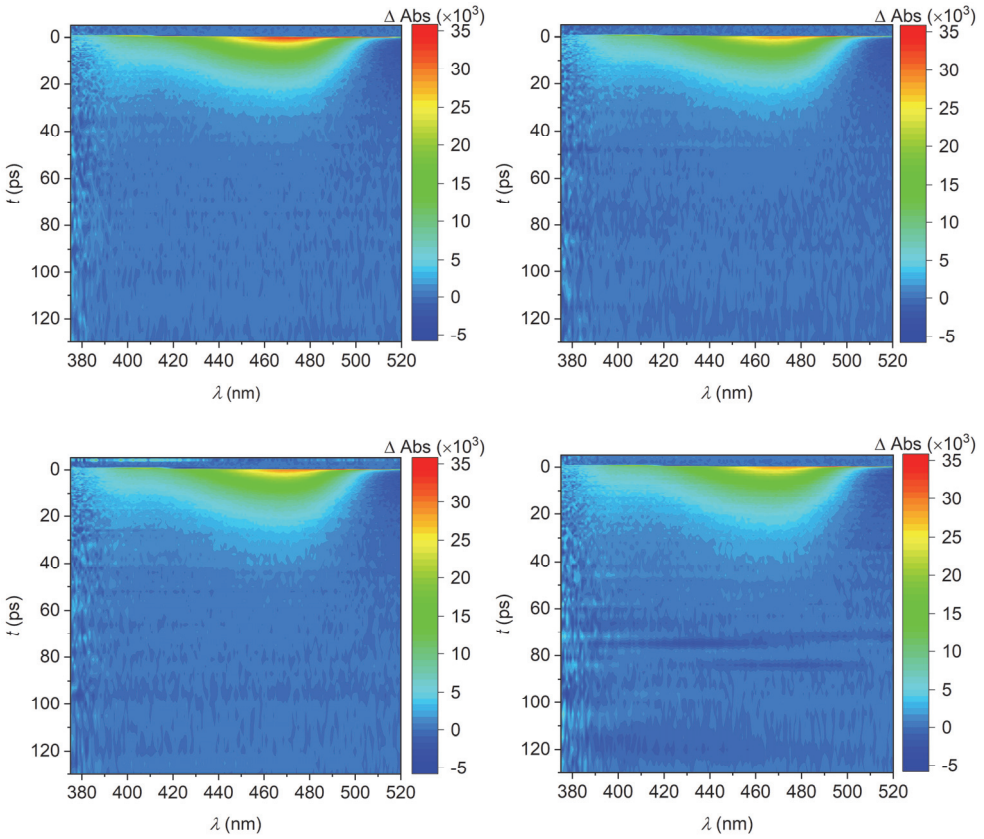

Figure E18. Duplicate transient absorption spectra obtained for (top) (*E*)-**2** + TFA (470 equiv.) and (bottom) (*E*)-**2** + TFA-d_1 (470 equiv.).

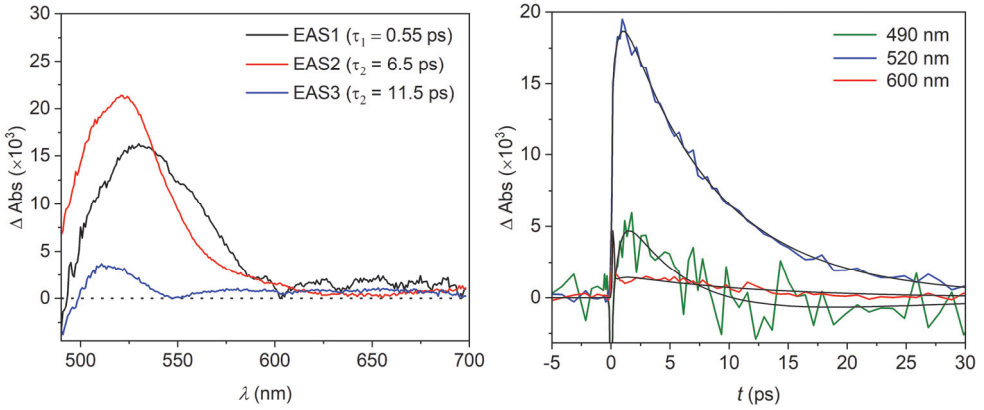

Figure E19. (left) representative evolution associated spectra (EAS) and their associated time constants of (*Z*)-**2**. (right) Kinetic traces with the fit (black line) as obtained by global analysis of the whole transient data matrix of (*Z*)-**2**.

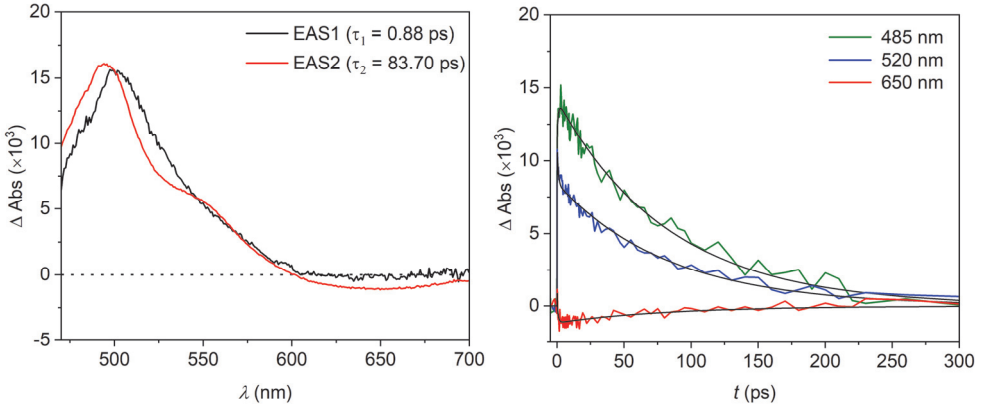

Figure E20. (left) representative evolution associated spectra (EAS) and their associated time constants of (*Z*)-**2** + **TFA**. (right) Kinetic traces with the fit (black line) as obtained by global analysis of the whole transient data matrix of (*Z*)-**2** + **TFA**.

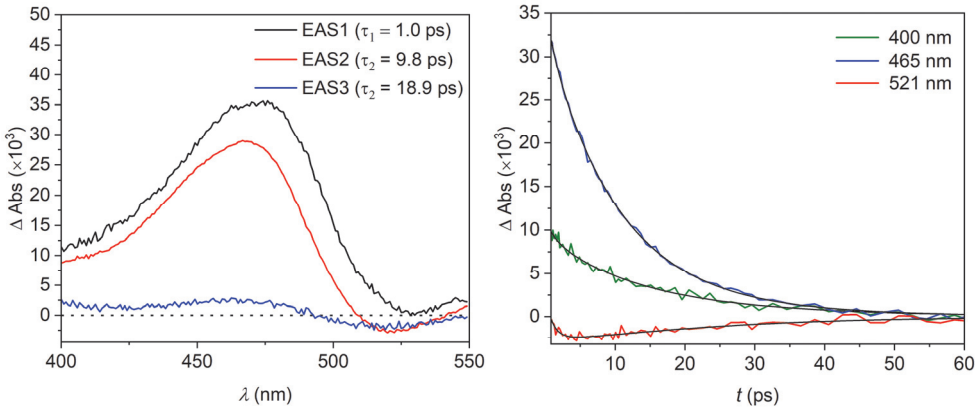

Figure E21. (left) representative evolution associated spectra (EAS) and their associated time constants of (*E*)-**2** + **TFA**. (right) Kinetic traces with the fit (black line) as obtained by global analysis of the whole transient data matrix of (*E*)-**2** + **TFA**.

Fluorescence Spectroscopy

Fluorescence emission and excitation spectra were recorded on a SPEX Fluorolog 3 fluorometer using a previously reported set-up[41] with double grating monochromators in both the excitation and emission channels, a Xenon excitation light source (450 W, Osram), and a Peltier cooled photomultiplier tube (Hamamatsu, R636-10). Spectra were corrected for the wavelength dependency of the excitation light intensity and the detector sensitivity. For emission spectra measurements, solutions of **1** and **2** were prepared in spectroscopy-grade CH_3CN such that maximum absorbance at the excitation wavelength (450 nm) was below ~ 0.2 in a 1 cm quartz cuvette, and for excitation spectra such that the absorbance at the maximum absorption wavelength was below ~ 0.1 in a 1 cm quartz cuvette.

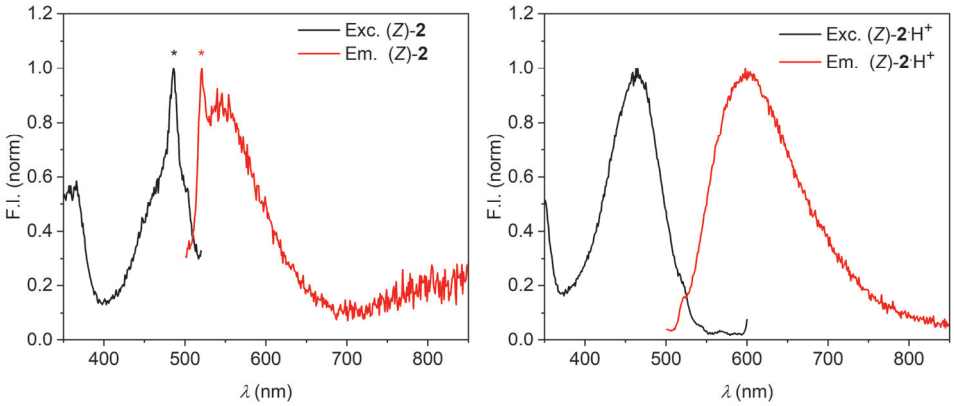

Figure E22. (left) Normalized excitation (λ_{em} = 570 nm, 7.1 μM (*Z*)-**2**) and emission (λ_{exc} = 450 nm, 25 μM (*Z*)-**2**) spectra in CH_3CN. (right) Normalized excitation (λ_{em} = 630 nm, 8.9 μM (*Z*)-**2**) and emission (λ_{exc} = 450 nm, 25 μM (*Z*)-**2**) spectra in CH_3CN. Peaks marked with * are due to Raman scattering (See Figure E23).

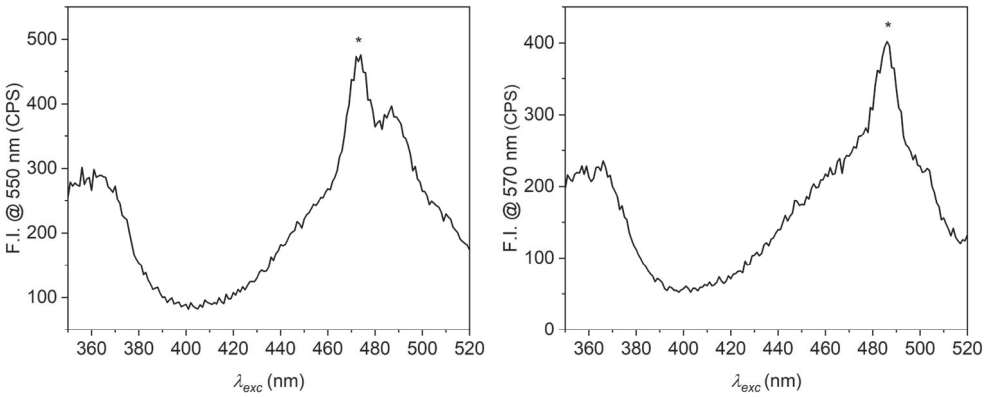

Figure E23. (left) Excitation spectrum following at λ_{em} = 550 nm or (right) following at λ_{em} = 570 nm of (*Z*)-**1** (8.9 μM). Peaks marked with * are due to Raman scattering. **Note**: the Raman scattering peak moves to longer wavelengths when the followed emission wavelength is increased.

Time Correlated Photon Counting

TCPC experiments were performed using a previously reported setup.[41] The excitation wavelength (450 nm) was produced by a tunable coherent Titanium:Sapphire laser (Chameleon Ultra). Fluorescence was detected using a multichannel plate photomultiplier tube (R3809-U-50, Hamamatsu), through a single-grating monochromator. The time-traces were fitted with IgorPro using a separately measured instrument response function obtained by monitoring the scattering of the excitation wavelength from a solution of colloidal silica.

Solutions were prepared in CH_3CN with an absorbance at the excitation wavelength of ~ 0.5 in a 1 cm cuvette. UV-Vis spectra were measured before and after each transient absorption

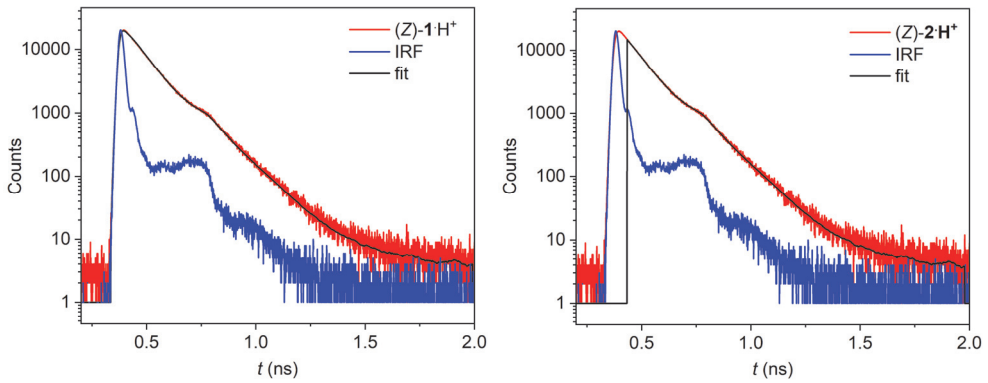

Figure E24. (left) Representative fit of TCSPC data of (*Z*)-**1** (77 μM) in the presence of TFA (470 equiv.). (right) Representative fit of TCSPC data of (*Z*)-**2** (81 μM) in the presence of TFA (470 equiv.).

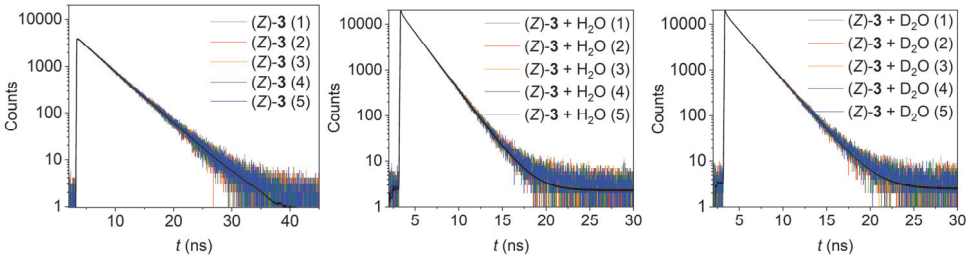

Figure E25. Fluorescence lifetime determination of (*Z*)-**3** (90 μM) with TCSPC in (left) pure CH_3CN (middle) in the presence of 0.1 v% H_2O (right) or in the presence of 0.1 v% D_2O.

Time-Dependent Density Functional Theory Calculations

All calculations were performed using Gaussian 16[4], and data was visualized using Avogadro 1.2.0[5] and Gaussview 6[6]. Geometry optimizations and relaxed scans on the ground-state structures were performed at the B3LYP/6-311++G(d,p) and CAM-B3LYP/6-311++G(d,p) level of theory including an IEFPCM solvation model (CH_3CN). All computed stationary points were subjected to frequency analysis and confirmed as local minima (no imaginary frequencies found for all minima). TD-DFT calculations were performed at the B3LYP/6-311++G(d,p) level of theory with an IEFPCM solvation model (CH_3CN), solving for the first 30 singlet excited-states and optimizing the geometry of the first excited state.

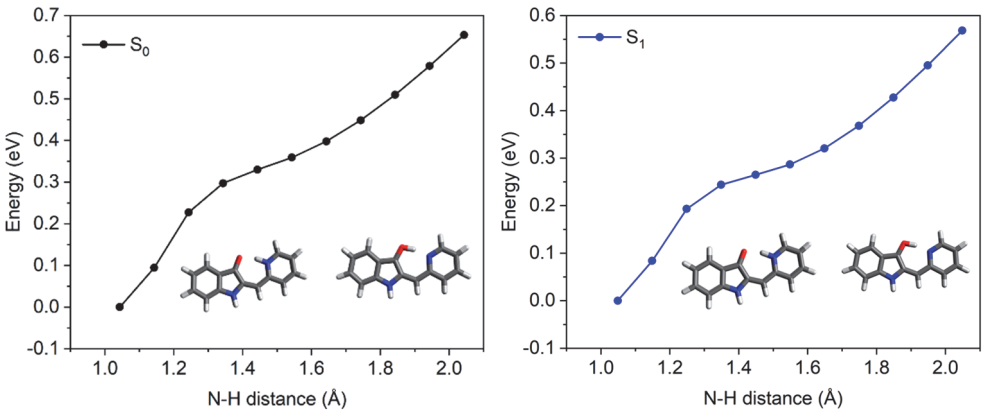

Figure E26. (left) Relaxed scan along the N-H distance of (*E*)-**1** on the S_0 PES (B3LYP/6-311++G(d,p)) (right) Relaxed scan along the N-H distance of (*E*)-**1** on the S_1 PES (CAM-B3LYP/6-311++G(d,p)).

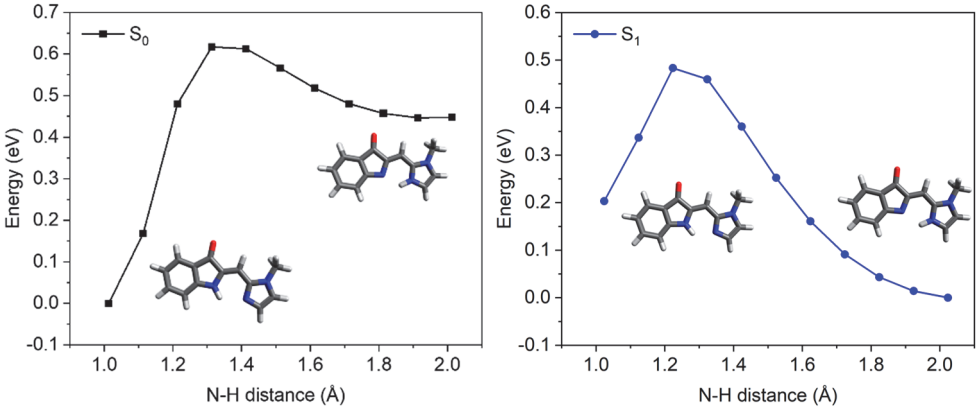

Figure E27. (left) Relaxed scan along the N-H distance of (*Z*)-**2** on the S_0 PES (B3LYP/6-311++G(d,p)) (right) Relaxed scan along the N-H distance of (*Z*)-**2** on the S_1 PES (CAM-B3LYP/6-311++G(d,p)).

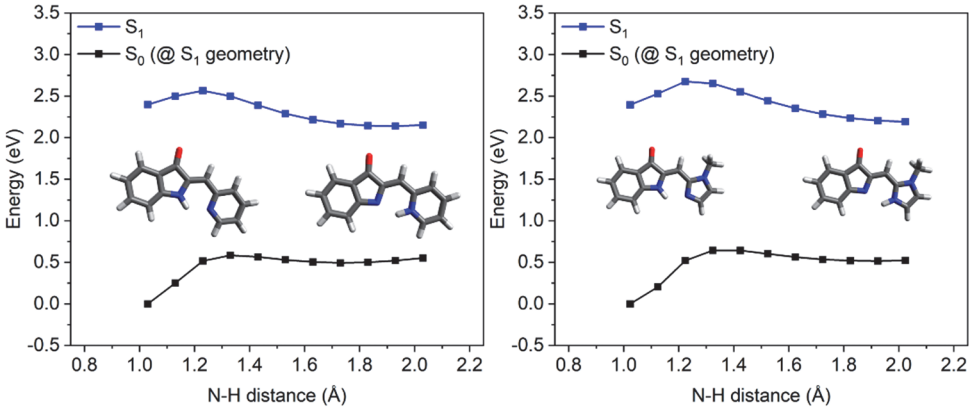

Figure E28. (left) Relaxed scan along the N-H distance of (*Z*)-**1** on the S_1 PES (CAM-B3LYP/6-311++G(d,p)) and the corresponding single point energies on the S_0 surface (at the S_1 optimized geometry). (right) Relaxed scan along the N-H distance of (*Z*)-**2** on the S_1 PES (CAM-B3LYP/6-311++G(d,p)) and the corresponding single point energies on the S_0 surface (at the S_1 optimized geometry).

$$k = \frac{k_B T}{h} e^{-\frac{\Delta G^{\ddagger}}{RT}} \qquad \text{(Eq. E2)}$$

The rates of proton transfer were then approximated using transition state theory using equation Eq. E2.

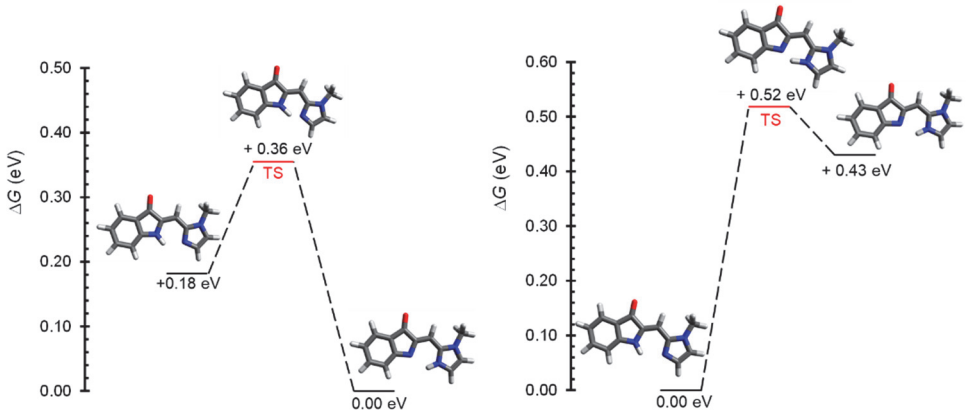

Figure E29. (left) Energy minimized geometry of the two tautomeric local minima of (Z)-**2** and the associated transition state on the S_0 PES alongside their relative Gibbs free energies (B3LYP/6-311++G(d,p)) (right) Energy minimized geometry of the two tautomeric local minima of (*Z*)-**2** and the associated transition state on the S_1 PES alongside their relative Gibbs free energies (CAM-B3LYP/6-311++G(d,p)).

Predicted vertical transition energies

Note that the deviation between computational prediction and experimentally observed excitation energies are expected to be around 0.25 eV.[42]

Table E1. The S_0 to S_1 vertical excitation energies as calculated by TD-DFT (CAM-B3LYP, 6-311++G(d,p), IEFPCM CH_3CN) alongside the oscillator strength (*f*) and the experimental maximum absorption wavelength (λ_{max}).

Compound	S_1 (eV/nm)	*f*	Exp. λ_{max} (eV/nm)
(*Z*)-**1**	2.85 / 436	0.32	2.58 / 480
(*Z*)-**1T**	2.19 / 565	0.31	-
(*Z*)-**1**·H^+	2.83 / 438	0.35	2.55 / 485
(*E*)-**1**·H^+	2.58 / 481	0.20	2.33 / 533
(*Z*)-**2**	2.82 / 439	0.37	2.55 / 485
(*Z*)-**2T**	2.20 / 564	0.23	-

Table E2. The S_0 to S_1 vertical excitation energies from the optimized S_1 geometry calculated by TD-DFT (CAM-B3LYP, 6-311++G(d,p), IEFPCM CH_3CN) alongside the oscillator strength (*f*) and the experimental wavelength of maximum fluorescence emission ($\lambda_{max,fl}$).

Compound	S_1 (eV/nm)	*f*	Exp $\lambda_{max,fl}$ (eV/nm)
(*Z*)-**1**	2.40 / 517	0.42	2.24 / 554
(*Z*)-**1T**	1.62 / 763	0.29	-
(*Z*)-**1**·H^+	2.24 / 554	0.35	1.98 / 625
(*E*)-**1**·H^+	2.10 / 590	0.21	-
(*Z*)-**2**	2.39 / 518	0.58	2.27 / 546
(*Z*)-**2T**	1.66 / 748	0.20	-

QM/MM Calculations

The computational methods described here were adapted from[10,43] with a slight modification. Geometry optimizations were performed at the Møller-Plesset perturbation theory-second Order (MP2)/6-31G*[44–46] level of theory with an implicit acetonitrile (CH_3CN) solvent in a Polarizable Continuum Model (PCM),[47] using Gaussian03 software package. Now, the atomic charges of the of protonated *Z* and *E* chromophores were obtained using the Second Order Electrostatic Potential Fitting (ESPF) method starting from the MP2/6-31G* data), while the bonding and van der Waals parameters were from the OPLS-AA force field.[48] Then, the (*Z*)-**1**·H^+ and (*E*)-**1**·H^+ were placed in the center of cubic box of size 60 x 60 x 60 Å with a total of 620 MeCN molecules. Then, the energy of the system was minimized at the molecular mechanics (MM) level using the conjugated-gradient method with periodic boundary conditions (PBC) while the chromophore is frozen. The minimized energy, in the above, was then relaxed for 5000 ps long at the molecular mechanics/molecular dynamics (MM/MD) simulation under the isothermal-isobaric ensemble (NPT) set at 1 atm and 298 K using the GROMACS software package.[49] During the first 300 ps of the simulation, the system was gradually thermalized to 298 K, equilibrated for the next 700 ps and sampled for the next 4000 ps. From the latter 4000 ps dynamic simulation step (i.e. the "production" step), 400 uncorrelated snapshots were extracted at every 10 ps and assumed to be representative of the thermal equilibrium Boltzmann distribution sample. The MeCN molecules located within 4 Å from any atom of hemi-indigo switches treated at the MM level were allowed to relax during QM/MM molecular dynamics while the rest of the MeCN molecules were kept frozen

(Figure 13). Each snapshot comprised a 20 Å solvent sphere (22 MeCN molecules) used in the construction of the QM/MM models (Figure 13). In the following computations, a frozen boundary approach[50,51] was used to keep the distribution of MeCN molecules fixed within the boundary layer. These 400 uncorrelated snapshots (geometries) are now used for the generation of the initial conditions necessary to compute the vertical excitation energies (VEEs) and simulate the UV-Vis absorption spectra as well as used for simulation of the S_1 photodynamics.

Following the computation of vertical excitation energies using 400 geometries, non-adiabatic excited-state dynamics (NAMD) simulations were conducted using Tully's surface hopping (SH) algorithm at the SA3 CAS-SCF/6-31G*/OPLS-AA level of theory. To highlight the role of conical intersections (CoIn) in the NAMD simulation of (*Z*)-**1**·H$^+$ and (*E*)-**1**·H$^+$, a comprehensive analysis of individual trajectories with extended simulation time would be required. In this work, however, to elucidate the mechanistic aspects of (Z)-**1**·H$^+$ and (*E*)-**1**·H$^+$, we mapped the potential energy surfaces shown in Figures 14 and 15. All geometry optimizations were performed at the SA3 CAS-SCF//SS-CASPT2/6-31G* level of theory. CoIn geometry optimizations were carried out by extracting snapshots from the S_0/S_1 hopping points observed in the NAMD simulation, followed by geometry optimizations on both S_0 and S_1 states and an analysis of the main dihedral angles. While all geometry optimizations were performed at SA3 CAS-SCF/6-31G*, to consider the electron correlation, the corresponding energies were corrected using the SA3 RMS-CASPT2/6-31G* level of theory.

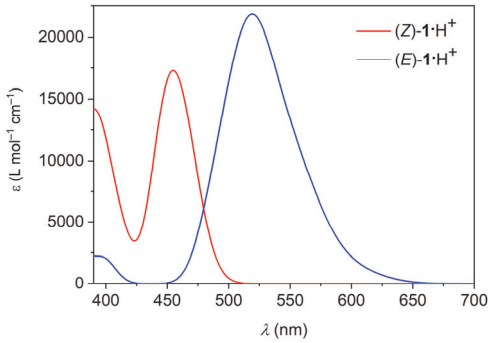

Figure E30. Simulated absorption bands by performing vertical excitation energies of the 400 geometries at the SA3-CASPT2/6-31G*(12e, 11o) level of theory.

Table E3. Comparison of simulated (SA3-CASPT2/6-31G*(12e, 11o)) and experimental λ_{max} (nm).

Compound	Sim λ_{max} (nm)	Exp λ_{max} (nm)
(*Z*)-**1**·**H**$^+$	470	485
(*E*)-**1**·**H**$^+$	520	533

3.9 References

[1] M. J. Fuchter, *J. Med. Chem.* **2020**, *63*, 11436–11447.

[2] B. L. Feringa, W. R. Browne (Eds.), *Molecular Switches*, Wiley-VCH, Weinheim, **2011**.

[3] M. Russew, S. Hecht, *Adv. Mater.* **2010**, *22*, 3348–3360.

[4] J. M. Abendroth, O. S. Bushuyev, P. S. Weiss, C. J. Barrett, *ACS Nano* **2015**, *9*, 7746–7768.

[5] J. D. Harris, M. J. Moran, I. Aprahamian, *Proc. Natl. Acad. Sci. U. S. A.* **2018**, *115*, 9414–9422.

[6] Z. L. Pianowski (Ed.), *Molecular Photoswitches: Chemistry, Properties, and Applications*, Wiley-VCH, Weinheim, **2022**.

[7] L. Greb, J.-M. Lehn, *J. Am. Chem. Soc.* **2014**, *136*, 13114–13117.

[8] N. Koumura, E. M. Geertsema, A. Meetsma, B. L. Feringa, *J. Am. Chem. Soc.* **2000**, *122*, 12005–12006.

[9] N. Koumura, R. W. J. Zijlstra, R. A. van Delden, N. Harada, B. L. Feringa, *Nature* **1999**, *401*, 152–155.

[10] M. Filatov, M. Paolino, R. Pierron, A. Cappelli, G. Giorgi, J. Léonard, M. Huix-Rotllant, N. Ferré, X. Yang, D. Kaliakin, A. Blanco-González, M. Olivucci, *Nat. Commun.* **2022**, *13*, 6433.

[11] I. M. Bekaert, M. A. Siegler, S. J. Wezenberg, *Org. Lett.* **2025**, *27*, 3612–3616.

[12] J. Gurke, Š. Budzák, B. M. Schmidt, D. Jacquemin, S. Hecht, *Angew. Chem. Int. Ed.* **2018**, *57*, 4797–4801.

[13] V. Serreli, C.-F. Lee, E. R. Kay, D. A. Leigh, *Nature* **2007**, *445*, 523–527.

[14] M. Kathan, S. Hecht, *Chem. Soc. Rev.* **2017**, *46*, 5536–5550.

[15] S. J. Wezenberg, *Chem. Commun.* **2022**, *58*, 11045–11058

[16] M. Dittmann, F. F. Graupner, B. Maerz, S. Oesterling, R. de Vivie-Riedle, W. Zinth, M. Engelhard, W. Lüttke, *Angew. Chem. Int. Ed.* **2014**, *53*, 591–594.

[17] N. Duindam, M. van Dongen, M. A. Siegler, S. J. Wezenberg, *J. Am. Chem. Soc.* **2023**, *145*, 21020–21026.

[18] V. Josef, F. Hampel, H. Dube, *Angew. Chem. Int. Ed.* **2022**, *61*, e202115512.

[19] M. Krell-Jørgensen, H. Zulfikri, M. G. Bonnevie, F. S. Bro, A. O. Dohn, L. Laraia, *Chem. Commun.* **2023**, *59*, 5278–5281.

[20] J. Pina, D. Sarmento, M. Accoto, P. L. Gentili, L. Vaccaro, A. Galvão, J. S. Seixas de Melo, *J. Phys. Chem. B* **2017**, *121*, 2308–2318.

[21] M. Ikegami, T. Suzuki, Y. Kaneko, T. Arai, *Mol. Cryst. Liq. Cryst.* **2000**, *345*, 113–118.

[22] T. Arai, M. Ikegami, *Chem. Lett.* **1999**, *28*, 965–966.

[23] M. Ikegami, T. Arai, *Bull. Chem. Soc. Jpn.* **2003**, *76*, 1783–1792.

[24] G. Cui, W. Thiel, *Phys. Chem. Chem. Phys.* **2012**, *14*, 12378–12384.

[25] S. Yamazaki, A. L. Sobolewski, W. Domcke, *Phys. Chem. Chem. Phys.* **2011**, *13*, 1618–1628

[26] I. Iwakura, A. Yabushita, T. Kobayashi, *Chem. Phys. Lett.* **2010**, *484*, 354–357.
[27] C. Hillel, S. Rough, C. J. Barrett, W. J. Pietro, O. Mermut *Commun. Chem.* **2024**, *7*, 250.
[28] D. Brynn Hibbert, P. Thordarson, *Chem. Commun.* **2016**, *52*, 12792–12805.
[29] J. J. Snellenburg, S. Laptenok, R. Seger, K. M. Mullen, I. H. M. van Stokkum, *J. Stat. Softw.* **2012**, *49*, 1–22.
[30] I. H. M. van Stokkum, D. S. Larsen, R. van Grondelle, *Biochim. Biophys. Acta, Bioenerg.* **2004**, *1657*, 82–104.
[31] T. Cohen, N. Svadlenak, C. Smith, K. Vo, S.-Y. Lee, A. Parejo-Vidal, J. R. A. Kincaid, A. L. Sobolewski, M. F. Rode, M. S. de Vries, *Eur. Phys. J. D* **2023**, *77*, 168.
[32] G. R. Han, D. Hwang, S. Lee, J. W. Lee, E. Lim, J. Heo, S. K. Kim, *Sci. Rep.* **2017**, *7*, 3863.
[33] X. Zhao, S. Yang, *J. Lumin.* **2020**, *220*, 116993.
[34] Y. Boeije, M. Olivucci, *Chem. Soc. Rev.* **2023**, *52*, 2643–2687.
[35] K. Das, D. S. English, J. W. Petrich, *J. Phys. Chem. A* **1997**, *101*, 3241–3245.
[36] W. Frey, F. Laermer, T. Elsaesser, *J. Phys. Chem.* **1991**, *95*, 10391–10395.
[37] M. Montalti, A. Credi, L. Prodi, M. T. Gandolfi, *Handbook of Photochemistry*, CRC Press, Boca Raton, **2006**.
[38] J. Rabani, H. Mamane, D. Pousty, J. R. Bolton, *Photochem. Photobiol.* **2021**, *97*, 873–902.
[39] C. H. Langford, C. A. Holubov, *Inorg. Chim. Acta* **1981**, *53*, 59–60.
[40] J. Sheng, W. Danowski, A. S. Sardjan, J. Hou, S. Crespi, A. Ryabchun, M. P. Domínguez, W. J. Buma, W. R. Browne, B. L. Feringa, *Nat. Chem.* **2024**, *16*, 1330–1338.
[41] T. Kumpulainen, B. H. Bakker, A. M. Brouwer, *Phys. Chem. Chem. Phys.* **2015**, *17*, 20715–20724.
[42] A. D. Laurent, D. Jacquemin, *Int. J. Quantum Chem.* **2013**, *113*, 2019–2039.
[43] M. S. Bezabih, D. S. Kaliakin, A. Blanco-González, L. Barneschi, A. N. Tarnovsky, M. Olivucci, *J. Phys. Chem. B* **2023**, *127*, 10871–10879.
[44] R. Krishnan, J. S. Binkley, R. Seeger, J. A. Pople, *J. Chem. Phys.* **1980**, *72*, 650–654.
[45] M. J. Frisch, M. Head-Gordon, J. A. Pople, *Chem. Phys. Lett.* **1990**, *166*, 275–280.
[46] M. Head-Gordon, J. A. Pople, M. J. Frisch, *Chem. Phys. Lett.* **1988**, *153*, 503–506.
[47] J. Tomasi, B. Mennucci, R. Cammi, *Chem. Rev.* **2005**, *105*, 2999–3093.
[48] C. Caleman, P. J. van Maaren, M. Hong, J. S. Hub, L. T. Costa, D. van der Spoel, *J. Chem. Theory Comput.* **2012**, *8*, 61–74.
[49] S. Pronk, S. Páll, R. Schulz, P. Larsson, P. Bjelkmar, R. Apostolov, M. R. Shirts, J. C. Smith, P. M. Kasson, D. van der Spoel, B. Hess, E. Lindahl, *Bioinformatics* **2013**, *29*, 845–854.
[50] S. Kawai, F. F. Canova, T. Glatzel, A. S. Foster, E. Meyer, *Phys. Rev. B* **2011**, *84*, 115415.

[51] C. R. Aldaz, T. J. Martinez, P. M. Zimmerman, *J. Phys. Chem. A* **2020**, *124*, 8897–8906.